JOURNAL OF GEOPHYSICAL RESEARCH, VOL. 113, E07001, doi:10.1029/2007JE002950, 2008

Ferric oxides in East Candor Chasma, Valles Marineris (Mars) inferred from analysis of OMEGA/Mars Express data: Identification and geological interpretation

Laetitia Le Deit,[1] Stéphane Le Mouélic,[1] Olivier Bourgeois,[1] Jean-Philippe Combe,[2] Daniel Mège,[1] Christophe Sotin,[1,3] Aline Gendrin,[4] Ernst Hauber,[5] Nicolas Mangold,[1,6] and Jean-Pierre Bibring[4]

Received 6 June 2007; revised 15 January 2008; accepted 21 February 2008; published 1 July 2008.

[1] The mineralogical composition of the Martian surface is constrained by analyzing the data of the OMEGA visible and near infrared imaging spectrometer onboard Mars Express. Ferric signatures had previously been reported in Valles Marineris, Margaritifer Terra, and Terra Meridiani. Here we use three independent data reduction methods (Spectral Angle Mapper, a modified Spectral Mixture Analysis and Modified Gaussian Model) to detect and map ferric oxides in East Candor Chasma, a part of Valles Marineris. Ferric oxides in East Candor Chasma are concentrated in scattered formations. MOLA altimetry indicates that the ferric oxides are preferentially located in topographic lows. THEMIS, HRSC and MOC images show that the ferric oxide spectral signatures are systematically correlated with superficial deposits of low albedo, located at the foot of, or resting on Interior Layered Deposits (ILDs). This spatial distribution suggests that ferric oxides are genetically linked to ILDs. Gravity and wind-driven remobilization of ferric oxides previously formed in the ILDs can explain their accumulation around the ILDs.

Citation: Le Deit, L., S. Le Mouélic, O. Bourgeois, J.-P. Combe, D. Mège, C. Sotin, A. Gendrin, E. Hauber, N. Mangold, and J.-P. Bibring (2008), Ferric oxides in East Candor Chasma, Valles Marineris (Mars) inferred from analysis of OMEGA/Mars Express data: Identification and geological interpretation, *J. Geophys. Res.*, *113*, E07001, doi:10.1029/2007JE002950.

1. Introduction

[2] Since January 2004, the OMEGA (Observatoire pour la Minéralogie, l'Eau, les Glaces et l'Activité) imaging spectrometer onboard Mars Express has revealed the presence of various minerals at the surface of Mars [*Bibring et al.*, 2005, 2006]. Most of the surface has been observed with a spatial resolution varying from 4.8 km/pixel to 0.3 km/pixel. Ferric oxide signatures have been identified in Valles Marineris, Margaritifer Terra, and Terra Meridiani in association with sulfate signatures [*Gendrin et al.*, 2005a, 2005b; *Bibring et al.*, 2007]. From a detailed and localized in situ analysis, the Opportunity rover has observed the presence of coarse-grained ferric-rich materials, which are associated with spherules of primarily gray hematite in Meridiani Planum [*Klingelhöfer et al.*, 2004; *Bell et al.*, 2004; *Squyres and Knoll*, 2005; *Calvin et al.*, 2004]. From orbit, thermal infrared mapping by Thermal Emission Spectrometer (TES), which has a nominal spatial resolution of 3.15 km [*Christensen et al.*, 1992], has revealed deposits of crystalline gray hematite exposed in Sinus Meridiani, Aram Chaos, and in numerous locations scattered throughout the Valles Marineris [*Christensen et al.*, 2001].

[3] On Earth, secondary minerals are alteration products that are formed under the action of various agents such as atmospheric changes, hydrothermal and biologic activity. Among these secondary minerals, ferric oxides are particularly important because they can form by aqueous alteration under specific temperature, pH, and Eh conditions, with various water contents [e.g., *King and McSween*, 2005]. Ferric oxides are thus a key element to constrain the paleoenvironmental conditions of Mars.

[4] We report here on a detailed study of ferric oxide signatures detected with OMEGA data in East Candor Chasma. This is a part of the Valles Marineris area, which formed by tectonic processes early in the Martian history. This depression has been filled with an extensive series of sedimentary rocks, commonly named Interior Layered Deposits (ILDs) which record the past geologic and climatic conditions of Mars. We use several analytical methods in order to obtain the maximum accuracy and confidence level in the distribution of ferric oxide minerals that occur in spatial association with the ILDs. Mineralog-

[1] Laboratoire de Planétologie et Géodynamique de Nantes, Université de Nantes, Nantes, France.
[2] Space Science Institute, Bear Fight Center, Winthrop, Washington, USA.
[3] Also at Jet Propulsion Laboratory and California Institute of Technology, Pasadena, California, USA.
[4] Institut d'Astrophysique Spatiale, Université Paris 11, Orsay Campus, France.
[5] Institute of Planetary Research, German Aerospace Center (DLR), Berlin, Germany.
[6] IDES, CNRS et Université Paris-Sud, Orsay Cedex, France.

0148-0227/08/2007JE002950$09.00

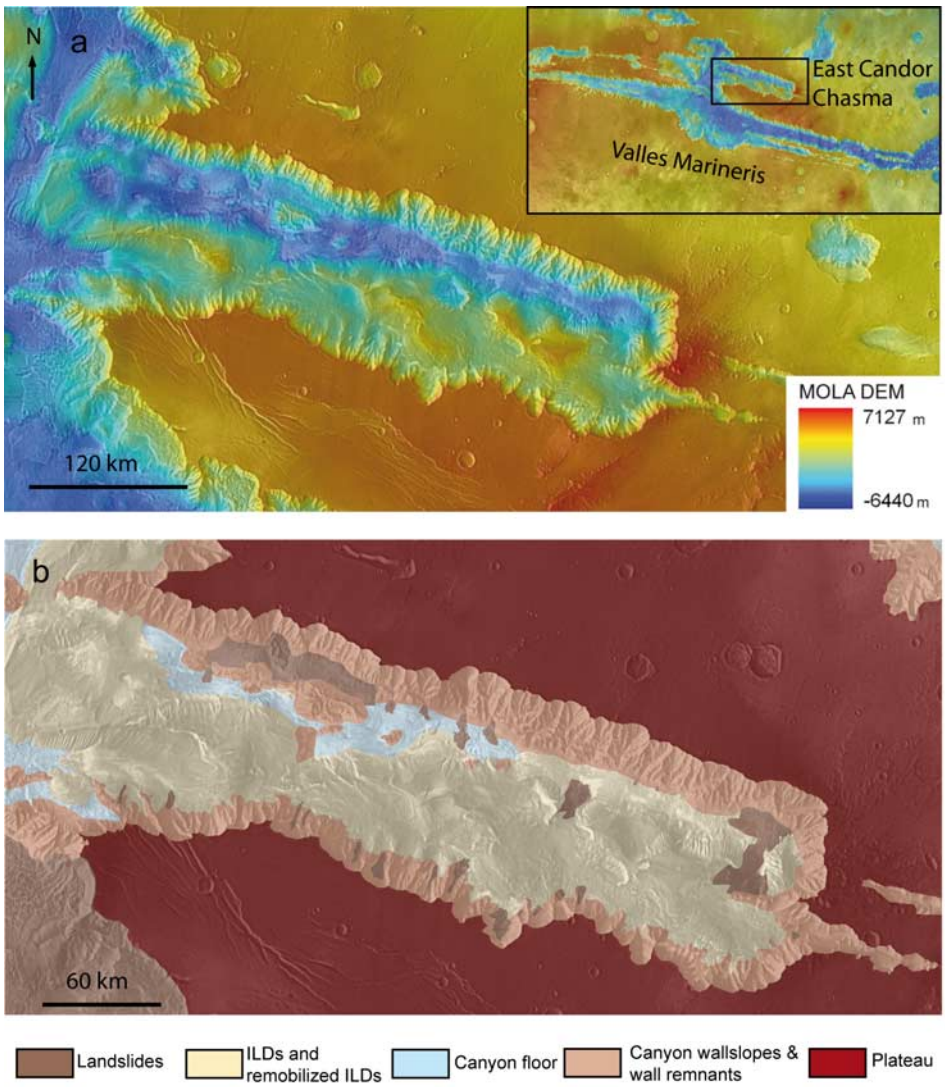

Figure 1. (a) Location of East Candor Chasma on Mars (63.5°W–72°W, 5°S–9°S). MOLA topographic map overlapping a mosaic of THEMIS IR images. (b) Simplified geologic map of East Candor Chasma, drawn from a mosaic of MOC, THEMIS, and HRSC images.

ical maps were derived using OMEGA data and were compared with topography and visible/IR images to characterize the geomorphologic context of the detected signatures. We use MOLA-derived digital elevation models (DEM), HRSC images, THEMIS visible and infrared images, MOC images, HiRISE images and TES spectral analysis results for this comparison. These data were combined in a Geographic Information System (GIS) in order to facilitate their analysis and to study their complementary aspects.

[5] First, we present the three methods of OMEGA data analysis used: Spectral Angle Mapper (SAM), Spectral Mixture Analysis (SMA) and Modified Gaussian Model (MGM). Then, we report on ferric oxide signatures that are inferred from these methods and we discuss the way of discriminating between confident and uncertain detections. In the next section we characterize the relation of ferric oxides with topography, the Interior Layered Deposits (ILDs), and sulfates. Finally, we discuss possible scenarios for the accumulation of ferric oxides in this area.

2. Study Area

[6] East Candor Chasma is one of the large Valles Marineris chasmata (Figure 1). It is more than 470 km long and 110 km wide. It is bounded by walls more than 6 km high, of which the initial spur and gully morphology has been locally reworked by mass wasting processes [e.g., *Peulvast et al.*, 2001]. The floor is covered by landslide deposits, layered deposits (Interior Layered Deposits, ILDs), and other sedimentary or volcano-sedimentary units [e.g., *Lucchitta et al.*, 1992; *Quantin et al.*, 2004]. Several origins have been proposed for the ILDs, including volcanic [*Lucchitta*, 1990; *Chapman and Tanaka*, 2001; *Komatsu et*

al., 2004], aeolian [*Nedell and Squyres*, 1987], and lacustrine [*Nedell and Squyres*, 1987; *McCauley et al.*, 1972] processes. Aeolian morphologies are common and include dunes and yardangs. ILDs are located in the central and southern portions of East Candor Chasma. The efficiency of aeolian erosion of the ILDs suggests that they are composed of rather loose or weakly indurated material.

3. Data and Methods

[7] We have reduced data from the OMEGA imaging spectrometer onboard Mars Express [*Bibring et al.*, 2004]. A reflectance spectrum between 0.38 μm and 5.2 μm is acquired for each pixel of an image. The instrument is composed of three detectors: VNIR (Visible Near Infrared) between 0.38 μm and 1.05 μm, SWIR (Short Wavelength InfraRed) between 0.93 μm and 2.73 μm, and LWIR (Long Wavelength InfraRed) between 2.55 μm and 5.2 μm. The contribution of the atmosphere is removed from each spectrum using an empirical atmospheric transmission derived from the ratio between two spectra acquired at the top and the bottom of Olympus Mons, and scaled to the depth of the 2 μm CO_2 band [*Langevin et al.*, 2005].

[8] An OMEGA spectrum is the result of a complex combination of several factors, partly because it is acquired remotely through the atmosphere. The shape of a spectrum varies mainly with the surface mineralogical components and their mixtures at both macroscales (areal mixtures) and microscales (intimate mixtures). In addition, it depends on the surface photometry due to texture and grain size variations, implying contributions from shading and scattering effects. The spectral shape also varies with the transparency of the atmosphere (amount of aerosols and their scattering properties) and the geometry of illumination and observations. Each data reduction method is aimed at extracting the mineralogical information alone, separate from atmospheric effects. Different methods have their own advantages and drawbacks and can be more or less sensitive to the various effects described above. Therefore we crosschecked three different data reduction methods in order to reduce the various effects and uncertainty of each one, so as to reinforce the confidence level in the detection and mapping of ferric oxides in East Candor Chasma.

[9] For the first two methods (Spectral Angle Mapper and Spectral Mixture Analysis), we focus on the SWIR detector data alone to avoid problems of spatial registration between VNIR and SWIR detectors. This approach was already adopted in other studies focused on sulfate identification [*Langevin et al.*, 2005; *Gendrin et al.*, 2005a, 2005b]. Although there is a specific ferric iron absorption centered at 0.9 μm, the typical sharp rise between 1.0 μm and 1.3 μm caused by the right wing of this broad band is very diagnostic for the detection of ferric oxides. It cannot be confused with the shape of the 0.9–1 μm band of pyroxenes, which is much narrower, with a right wing extending up to 1.1 μm only. It cannot be confused either with the 1 μm band of olivine, which tends to go out to 1.5 μm. For the third method (Modified Gaussian Model), we use both VNIR and SWIR detectors. In this case, a spatial registration correction is applied between both detectors. The three methods are applied to OMEGA data that provides nearly total coverage of the canyon (orbits number 308, 482, 515, 548, 1103, 1114, 1147, 1158, 1180, 1429, 1462, 1590, 1995, 2006, 2017, 2039, 2050, 2464).

3.1. Spectral Angle Mapper (SAM)

[10] The SAM is an algorithm designed to determine the similarity between spectra in a multidimensional space. Spectra are treated as vectors. Given a reference spectrum of reflectance R and the spectrum to analyze R′, the spectral angle α is formed between the two spectra and has a dimensionality equal to the number of bands N [*Kruse et al.*, 1993]. The spectral angle is defined by:

$$\alpha = \cos^{-1}\left(\frac{\sum_{\lambda=1}^{N} R_\lambda R'_\lambda}{\sqrt{\sum_{\lambda=1}^{N} R_\lambda^2}\sqrt{\sum_{\lambda=1}^{N} R_\lambda'^2}}\right) \quad (1)$$

[11] We take as reference an extreme spectrum (called an end-member) derived from an OMEGA mosaic of East Candor Chasma. We identified this end-member by using the spectral hourglass wizard implemented in the ENVI software. This processing pipeline includes a Minimum Noise Fraction transformation to reduce the spectral dimensionality, followed by the Pixel Purity Index (PPI) algorithm [*Boardman et al.*, 1995], and an examination of the result with the n-Dimensional visualization tool. The PPI algorithm is aimed at finding the most diverse areas in a given data set by mathematically pulling out the extreme spectra with high variance relative to the average for the region (end-member). Among these extreme spectra, one has spectral properties indicative of ferric oxides (Figure 2), with the characteristic steep positive slope ranging from 1 μm to 1.3 μm. The presence of a drop in reflectance near 2.4 μm may indicate that there is some sulfate or other hydrated material in the spectrum. However, a sulfate alone cannot account for the shape of the spectrum between 1 and 1.3 μm, which is well reproduced if an iron oxide is present. Some ferric sulfates such as schwertmannite could also display a broad 1 μm feature which mimics the one of iron oxides, but the global spectral shape is still quite different from what we observe in East Candor Chasma. This is why we favor a ferric oxide associated with a small amount of sulfate and not a ferric sulfate, even if it cannot be ruled out completely. The end-member corresponds to an area of dark-toned dunes at the base of a fresh cliff composed of stratified material (Figure 2c), which could account for the small component of sulfate.

[12] The spectral angle between the end-member and each pixel spectrum of the mosaic is then computed. Small spectral angles correspond to high similarity between the reference spectrum and the analyzed spectra of the image. The SAM algorithm is sensitive to the spectral shape at all wavelengths and takes into consideration variations of albedo and band depths between the spectra [*Combe*, 2005]. However, this method is sensitive to slope variations in the spectra. Therefore it might also be sensitive to effects of scattering on the surface and in the atmosphere by aerosols, which have not been removed from these data [*Combe*, 2005]. Therefore the map obtained by SAM will

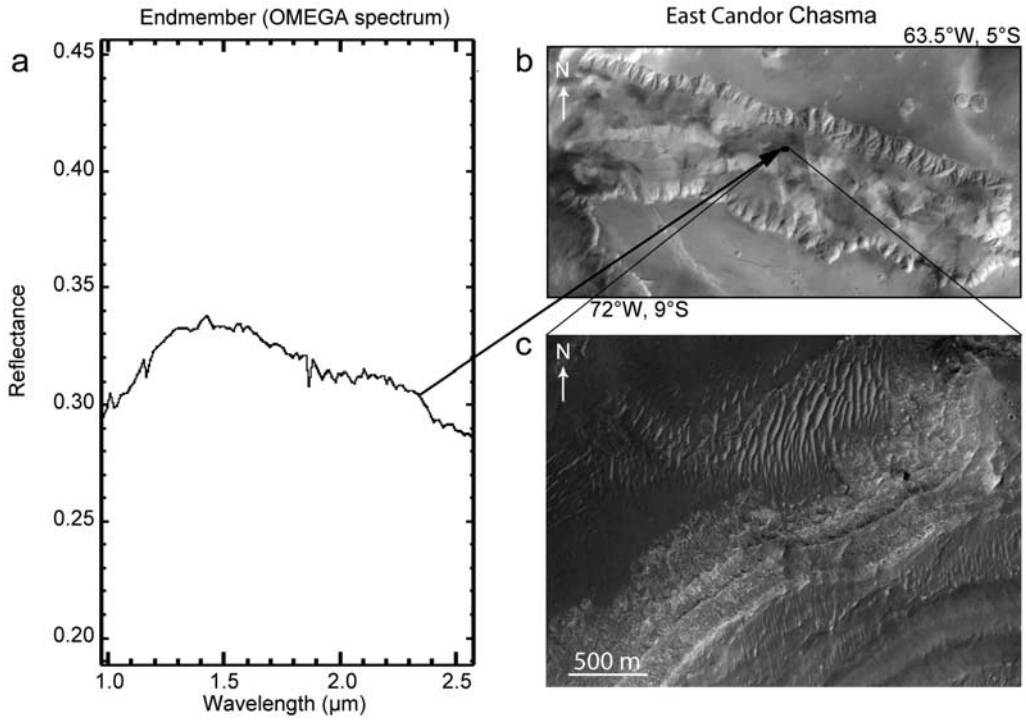

Figure 2. (a) OMEGA spectrum corresponding to the end-member provided by the PPI (Pixel Purity Index) tool, displaying spectral characteristics of ferric oxides. (b) MOC mosaic (64 pixels/degree). Black box: location of the pixel corresponding to the end-member and of the corresponding image shown in Figure 2c. (c) Portion of HiRISE image (PSP_002432_1730).

be cross-checked against the two other methods in the next section.

3.2. Spectral Mixture Analysis (SMA)

[13] The Spectral Mixture Analysis uses a least squares regression to find the linear combination of a suite of end-members that best matches the spectrum for each pixel of an image [*Boardman*, 1989, 1992; *Sabol et al.*, 1992; *Ramsey and Christensen*, 1998; *Mustard and Sunshine*, 1999]. It corresponds to the inversion, on a pixel by pixel basis, of the system $Y = AX$ where Y is a vector containing the OMEGA spectrum, A is a $N \times M$ matrix filled with the end-member spectra (with N the number of spectral channels and M the number of end-members) and X a vector containing the coefficients attributed to each end-member. We use the term ''mixing coefficient'' on purpose instead of the usual ''image fraction'' terminology often associated to SMA in the literature. The word fraction is not appropriate here because it refers to proportions, especially when SMA results are constrained to be less than one and their sum is set to be one. In the inversion process, negative coefficients may be obtained in X, which have no physical sense. In our linear unmixing approach [*Combe et al.*, 2008, 2006], end-members having negative coefficients are eliminated through an iterative process.

[14] The final accuracy of the linear fit is evaluated by computing the root mean square (RMS) error between the model and the data. This RMS error is often used as a measurement of the goodness of fit [e.g., *Clark and Swayze*, 1995].

[15] In our study, we use 24 laboratory spectra as input end-members. The main groups of rock-forming minerals are represented, such as high and low-calcium pyroxenes, olivines, phyllosilicates, sulfates, iron oxides and hydroxides and carbonates (Table 1). This reference library is built from two main data sets: the USGS speclib05 [*Clark et al.*, 2003] and measurements acquired to support the CRISM experiment [*Murchie et al.*, 2007a]. The spectra were measured on different spectrometers: a Beckman 5270 and a RELAB Nicolet 740 respectively. Measurements correspond to bidirectional reflectance acquired with an incidence angle of 30° and an emergence angle of 0°. Samples are powders or rock chips composed of minerals with various grain sizes (Table 1). In our approach, an artificial flat spectrum is also added to this library [*Combe et al.*, 2008]. It accounts for variations of illumination and surface scattering that are mainly due to surface roughness and grain size effects. Since the spectral library does not contain all possible grain sizes of surface materials, the present algorithm is set up so that mixing coefficients and the flat spectrum can account for grain size variations. For this purpose, coefficients are not constraint to be less than one, and their sum is not set to be one. Consequently, grain size effects like absorption band depth and global spectral level variations can be modeled. As a result, coefficients are indicative of the presence of materials but not of actual proportions. Two straight line spectra, one with a positive slope and the other a negative slope, are also included [*Combe et al.*, 2008]. These spectra account for possible variations in the continuum slope, which are mostly related to atmospheric scattering.

Table 1. Description of Mineral Samples Represented in the Spectral Library Used as Input for the SMA

Group of Rock-Forming Mineral	Mineral Name	Source of the Spectrum	Sample-ID	Sample Description (Particle Size (P. s.), Rock Ship or Powder, Purity of Sample)
Orthopyroxene	hypersthene	USGS	NMNHC2368	P. s. > 250 μm powder of pure pyroxene except for a small amount of tremolite (less than 2%)
Clinopyroxene	diopside	CRISM	CPX 75	25 μm < P. s. < 75 μm high calcium pyroxene from volcanic bomb
Olivine	fayalite	CRISM	OLV 112	P. s. < 45 μm sample somewhat oxidized
	forsterite	CRISM	OLV 003	P. s. < 45 μm
Phyllosilicates	kaolinite (clay)	CRISM	KAO 104	P. s. < 45 μm poorly ordered kaolinite
	smectite (clay)	CRISM	ILS 103	P. s. < 45 μm illite-smectite mixed layer
	montmorillonite (clay)	CRISM	MON 102	P. s. < 45 μm powdered bentonite
	illite (clay)	CRISM	acquired from ward's (sample #46E035)	P. s. < 45 μm (green shale)
	nontronite (clay)	CRISM	nontronite	125 μm < P. s. < 250 μm
	chlorite	CRISM	chlorite	P. s. < 125 μm
	muscovite (mica)	USGS	GDS 116 Tanzania	
	chrysotile (serpentine)	CRISM	clinochrysotile	untangled collection of string-like crystals
	lizardite (serpentine)	CRISM	lizardite	P. s. < 125 μm
Sulfates	alunite (Al-K rich)	USGS	GDS 83	P. s: 35 μm very little contamination
	jarosite (K-Fe rich)	CRISM	jarosite	orange mineral layers in rock
	kiserite (Mg- rich)	CRISM	kieserite purchased from Ward's	P. s. < 75 μm white powder, sieved
Polyhydrated sulfates	epsomite (Mg-rich)	USGS	GDS 149 spectrum originally published by *Crowley* [1991]	"epsom salts"
	gypsum (ca- rich)	CRISM	gypsum	25 μm < P. s. < 75 μm
Oxides and hydroxydes	hematite	CRISM	HEM 101	P. s. < 140 nm Synthetic hematite
	goethite	CRISM	goethite	P. s. < 125 μm
	ferrihydrite	USGS	GDS 75 (F6) samples made by Dave Sherman	Synthetic ferrihydrite
Carbonates	calcite	CRISM	CRB 112	45 μm < P. s. < 90 μm
	dolomite	CRISM	dolomite purchased from ward's	25 μm < P. s. < 75 μm Wet crystalline hand sample
Water	frost	JHU	FROST.SNW	P. s.: 10 μm

3.3. Modified Gaussian Model (MGM)

[16] The Modified Gaussian Model [*Sunshine et al.*, 1990] finds the best combination of Gaussians that fits the absorption bands in a given spectrum. This method is useful to identify absorption bands and to evaluate their variations. The method used in our study is similar to the one used by *Bibring et al.* [2007], with the input parameters described by *Mustard et al.* [1997]. We evaluated the spectra between 0.7 μm and 2.5 μm. The positions and widths of the absorption bands were fixed to reduce the computation time [*Gendrin et al.*, 2005a, 2005b].

4. Results

4.1. Identification of Ferric Oxides

[17] The three methods described above take different spectral properties into account. In order to minimize the possibility of inaccurate detections, the mineral maps obtained by each method are visually inspected and cross-checked against each other (Figure 3).

[18] Figure 3a shows a SAM classification of OMEGA images corresponding to the end-member of Figure 2, which has spectral characteristics of ferric oxides. Colored areas represent regions whose spectra have a high similarity with this end-member. The smaller the spectral angle, the higher the similarity between the spectra and the end-member is (darker tones in Figure 3a). Spectral angle values greater than 0.02 are not represented to avoid an over interpretation of the results. The 0.02 value provides a good trade off between detection capabilities and reliability. Figure 3b shows the distribution of ferric oxides detected by SMA. This map combines the detection of two ferric oxides from the input library (hematite + goethite). Indeed, whereas the input library contains spectra of goethite and hematite, the spectral shape of these two minerals do not differ markedly. We therefore consider that the identification provided by the linear mixing model is relevant for the oxide family, but not for the discrimination between hematite and goethite. This issue has also been raised by *Bibring et al.* [2007]. The discrimination between different types of ferric oxides within identified oxide deposits would require a more comprehensive set of laboratory data and is beyond the scope of this work. In the following, we used a sum of the two oxides contributions to produce an integrated ferric oxide map. Mixing coefficients of ferric oxides are high and range between 0.15 and 0.3, meaning that the ferric oxide end-members provide a major contribution to the mixing. Figure 3c represents the amplitude of the Gaussian fit to the ferric oxide absorption band centered at 0.9 μm. Only the highest amplitudes between 1 μm and 1.3 μm that are greater than 15% are selected. Such high spectral amplitudes in this wavelength range are characteristic of ferric oxides.

[19] Only the strongest spectral signatures, which indicate the most obvious mineralogical detections are presented. Thus only those with the smallest spectral angles, the

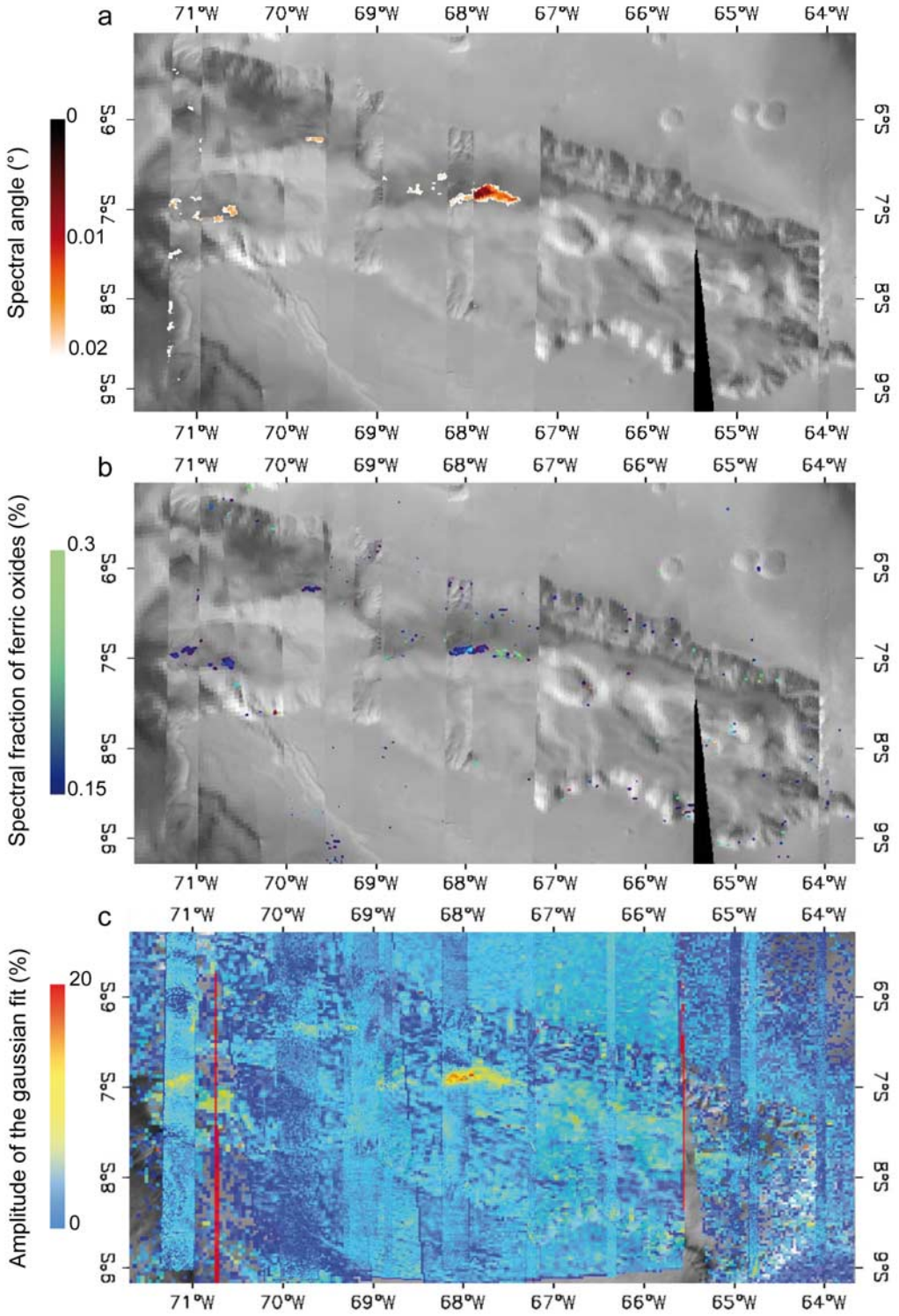

Figure 3. Distribution maps of ferric oxides in East Candor Chasma (63.5°W–72°W, 5°S–9°S) obtained with three methods of analysis of OMEGA data. (a) Spectral Angle Mapper. Spectral angle (in degree) between OMEGA spectra and the end-member with spectral characteristics of ferric oxides shown on Figure 2. Colored areas represent regions with a high spectral similarity with this end-member (spectral angle $\leq 0.02°$). (b) Spectral Mixing Analysis. Colors represent the mixing coefficient of ferric oxide in the overall spectrum. It is not absolute mineral proportion. (c) Amplitude of the MGM Gaussian fit to the ferric oxide absorption band centered at 0.9 μm. The deeper the Gaussian, the stronger the spectral signature is.

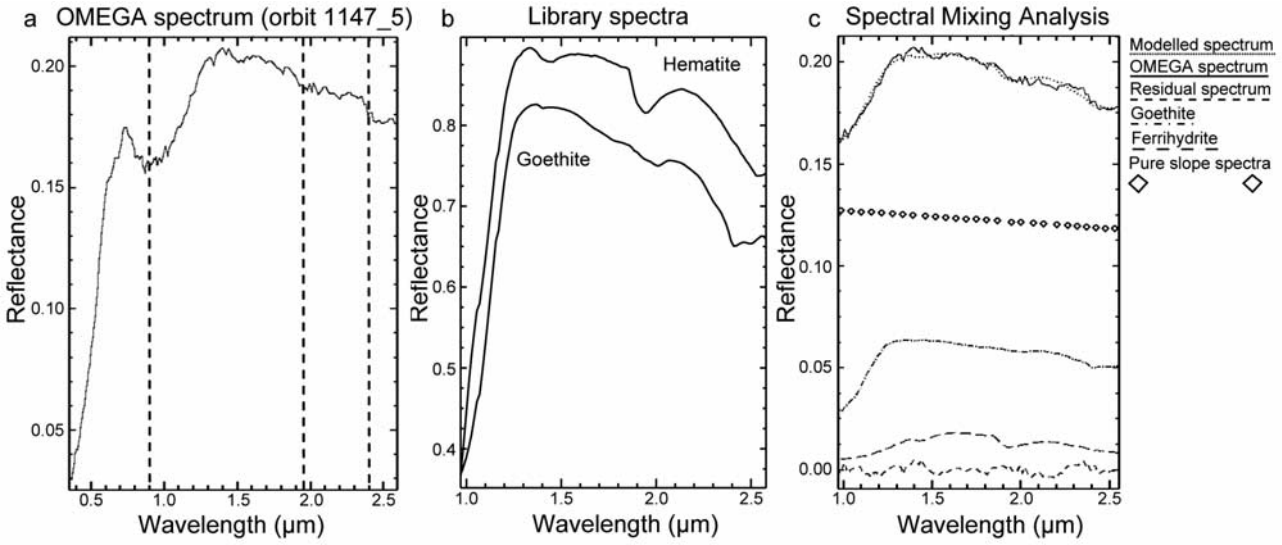

Figure 4. Spectral analysis of the area located in the central part of East Candor Chasma (292.3°E, 7°S). (a) OMEGA spectrum of a pixel showing a strong signature of ferric oxides. (b) Laboratory spectra of goethite and hematite used in the library [*Clark et al.*, 1993]. (c) OMEGA spectrum shown in Figure 4a and the corresponding spectrum modeled by the Spectral Mixing Analysis between 0.93 μm and 2.73 μm. The goethite end-member contributes the most to the observed mixed spectrum. Pure slope spectra correspond to the sum of three straight lines, one having a flat spectrum and others a negative and positive slope.

highest mixing coefficients, and the highest amplitudes of the Gaussians between 1 μm and 1.3 μm are shown. The quality of OMEGA data is also considered. Several factors can influence spectral detections and lead to false detections. The spatial resolution of images plays an important role in the detection capabilities (high spatial resolution gives access to more ''pure'' pixels, and therefore to stronger signatures). Transient atmospheric phenomena such as water ice clouds may sometimes affect the spectrum quality, in particular in the 1.5 and 2 μm regions. Aerosols, which correspond to dust particles in the atmosphere, can similarly mask surface spectral signatures. Finally, isolated pixels with high oxide contents may be spurious and represent noise within the results; therefore we have chosen to map only clusters of pixels in order to improve the confidence level of oxide detections.

[20] At the first order, the three methods are consistent but some discrepancies exist locally. Consequently, each of the detections has been studied in detail. As an example, all three analysis methods yield a large, crescent-shaped area with a spectral signature of ferric oxides at a site located in the central part of East Candor Chasma (Figure 3). A typical OMEGA spectrum of the area shows characteristics of ferric oxides with a deep band at 0.9 μm and a steep positive slope between 1 μm and 1.3 μm (Figure 4a). Library spectra of ferric oxides (hematite and goethite) are shown for comparison in Figure 4b. It should be noted that the small hydration feature at 1.9 μm in the hematite spectrum suggests that the laboratory sample is not composed of pure hematite. In Figure 4c, OMEGA spectrum of the crescent-shaped area in East Candor Chasma is compared with a spectrum modeled by SMA. The main contribution in the linear mixing model is the goethite end-member, followed by a small component of ferrihydrite. Therefore the SMA method confirms that ferric oxides are present in the area. According to Figure 3c, the amplitude of the Gaussian between 1 μm and 1.3 μm in the region reaches more than 20%, which also indicates a strong signature of ferric oxides. Finally, the ferric oxide signature is observed both at low and high spatial resolution (orbits 1147 and 1429). All these arguments suggest that this area is enriched in ferric oxides.

[21] After having analyzed the whole chasma, we have established two different confidence levels in the distribution map of ferric oxides by using mainly the redundancy of the three detection methods, followed by visual control of the individual spectra. The locations of the most robust detections are indicated in orange on Figure 5. These detections appear to be obvious according to the methods used and were obtained from high quality OMEGA data (absence of water ice cloud, low aerosols). The areas indicated in blue correspond to areas where the detection of ferric oxides still has to be confirmed with new data sets. These detections have been made by one or more of the mapping methods but are associated either with a low spectral signature or with a low quality of data. These sites could be of special interest for the CRISM imaging spectrometer onboard Mars Reconnaissance Orbiter, which has a maximum spatial resolution of ~18 m/pixel [*Murchie et al.*, 2003]. *Knudson et al.* [2007] already confirmed one of these detections in a preliminary analysis of CRISM data.

4.2. Correlations With Other Data Sets

[22] The sites enriched in ferric oxides in East Candor Chasma have been investigated using MOLA, HRSC, THEMIS, MOC, HiRISE, and TES data sets.

[23] The gridded 128 pixels/degree Mars Orbiter Laser Altimeter (MOLA) DEM provides the global topographic framework with a relative vertical accuracy of ~1 m [*Smith et al.*, 2001].

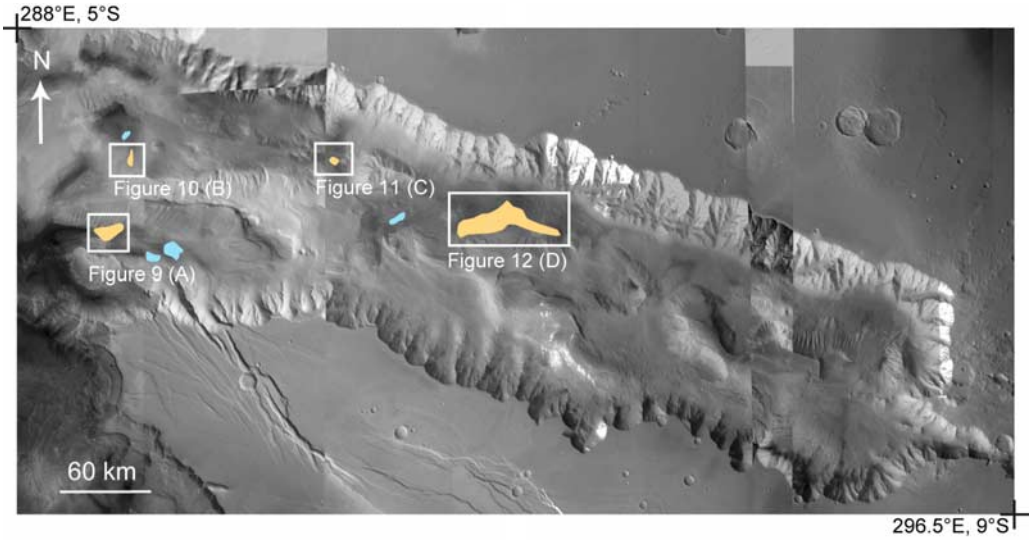

Figure 5. Location map of spectral signatures in East Candor Chasma (63.5°W–72°W, 5°S–9°S), superimposed on a mosaic of HRSC images. The three analysis methods used in this study take distinct spectral properties into account. This multimethod approach improves the detection confidence. Sites with robust detections are indicated in orange, sites where the detection of ferric oxides still has to be confirmed are indicated in blue. Locations of Figures 9, 10, 11, and 12 (corresponding to sites A, B, C, and D respectively) are indicated.

[24] The High Resolution Stereo Camera (HRSC) onboard Mars Express provides high spatial resolution panchromatic images, color images at 100 m per pixel and DEMs with an unprecedented lateral resolution of about 200 m per pixel [*Neukum and Jaumann*, 2004]. In this study, we focus on the nadir panchromatic images that have the best spatial resolution (12.5–30 m/pixel) (orbits 0334, 0515, 1984, 1995, 2006, 2017, 2028, and 2039).

[25] Daytime and nighttime infrared Thermal Emission Imaging System (THEMIS) data [*Christensen et al.*, 2004] have been useful for studying the thermal emissivity and geomorphology of the surface. At night, differences in surface temperature are essentially due to the thermal inertia of the surface materials because the effects of topography and albedo are reduced [e.g., *Kieffer et al.*, 1973]. Therefore nighttime infrared THEMIS data provide information on the ability of surface materials to retain the heat accumulated during daytime and is used to identify contrasts in the degree of induration and/or in the granulometry of surface materials. For instance, weakly indurated aeolian deposits are characterized by low thermal inertia, whereas outcrops of fresh competent rocks are characterized by high thermal inertia [*Mellon et al.*, 2000]. Infrared THEMIS images have a spatial resolution of 100 m/pixel. Daytime visible THEMIS images (18 m/pixel) have been used to interpret the geomorphology at a scale intermediate between THEMIS IR, HRSC, and MOC.

[26] Thermal Emission Spectrometer (TES/MGS) thermal inertia maps at a spatial resolution of 20 pixels per degree [*Putzig et al.*, 2005] have been used to evaluate thermal inertia of ferric-oxide rich areas and make interpretations about the geological properties of the surfaces. The thermal inertia unit is $Jm^{-2}\ K^{-1}\ s^{-1/2}$ and we will use the "SI" shorthand thereafter. We will also compare the distribution of gray crystalline hematite detected by TES with the distribution of ferric oxides obtained in the present study.

[27] With a spatial resolution as fine as 1.4 m/pixel [*Malin et al.*, 1992], the Mars Observer Camera (MOC) images have been used to constrain the detailed geomorphology of specific small areas. These data sets have been combined into a geographic information system using the Mars 2000 geographic coordinate system available in ArcGIS [*Seidelmann et al.*, 2002].

4.2.1. TES Thermal Inertia Map Analysis

[28] *Gendrin et al.* [2005a, 2005b] identified isolated sulfate signatures (monohydrated and polyhydrated sulfates) on the ILDs of East Candor Chasma (Figure 6a). The 2 μm band depth derived from an MGM analysis [e.g., *Mustard et al.*, 2005; *Bibring et al.*, 2005] allowed us to detect pyroxenes surrounding the ILDs on the chasma floor (Figure 6b). ILDs in East Candor Chasma are characterized by a large range of thermal inertia values (70–711 SI, with a mean of 240 SI, and most pixels between 130–300 SI) (Figures 6c and 7). These values have been derived from the TES thermal inertia map at 20 pixel-per-degree resolution (corresponding to ~3 km/pixel) [*Putzig et al.*, 2005]. Thermal inertia values < 200 SI suggest loose, fine surface dust and only few rock outcrops [*Mellon et al.*, 2000]. This implies that most parts of ILDs' surface may be mantled by dust, which prevents the detection of strong spectral signatures.

[29] However, thermal inertia values of the ferric oxide-rich sites ranges from 277 SI to 643 SI (485 SI on average) (Figures 6c and 7). Therefore these areas do not correspond to dusty surfaces and this type of strong ferric signature detected by OMEGA cannot correspond to fine-grained dust. Furthermore, the distribution of crystalline gray hematite detected by TES (Figure 8) is at the first order

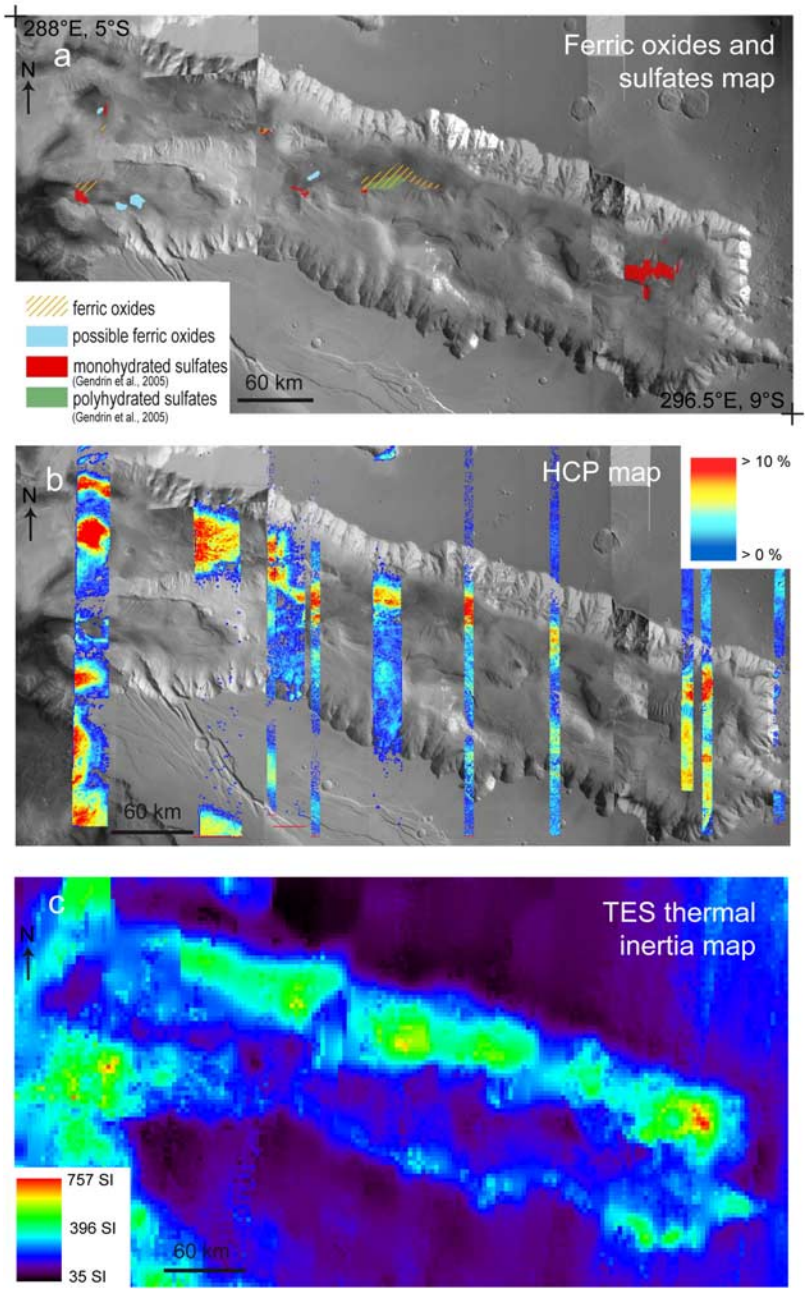

Figure 6. (a) Location map of ferric oxides and sulfates in East Candor Chasma (63.5°W–72°W, 5°S–9°S) plotted over a mosaic of HRSC images. Polyhydrated sulfates (in green) and monohydrated sulfates (possibly kieserite, in red) have been detected using band depth spectral parameters (1.9 μm–2.4 μm and 2.1 μm respectively). Polyhydrated sulfates may be iron, magnesium or sodium-rich. Ferric oxide-rich sites are found nearby sulfate-rich areas; this suggests that both families of minerals are genetically related. (b) High calcium pyroxene band depth map. Only high spatial resolution data are represented. (c) TES-derived thermal inertia map (20 pixels/degree) [*Putzig et al.*, 2005].

consistent with the distribution of ferric oxides in this study but some differences occur locally (Figure 5).

4.2.2. Analysis of Ferric Oxide-Rich Sites

[30] Site A (Figure 9) is 9.5 km long and 7 km wide. It is located in a topographic low between −2050 m and −4450 m (Figure 9a). It corresponds to terrains of heterogeneous albedo, though usually lower than the surrounding terrains (Figure 9b). A portion of the western part of the ferric oxide-rich site corresponds to a bright butte that differs from the major fraction of the area enriched in ferric oxides. The terrains north of site A are light-toned ILDs (Figures 9b and 9c), whereas those located to the SW consist of bright and dark material with a mottled appearance (Figure 9b). Calculation of the 2.1 μm band depth (Figure 6a) suggests that this latter feature may also contain monohydrated sulfates [*Gendrin et al.*, 2005a, 2005b]. Figure 9d shows part of a nighttime THEMIS infrared image. On this image, site A is generally characterized by

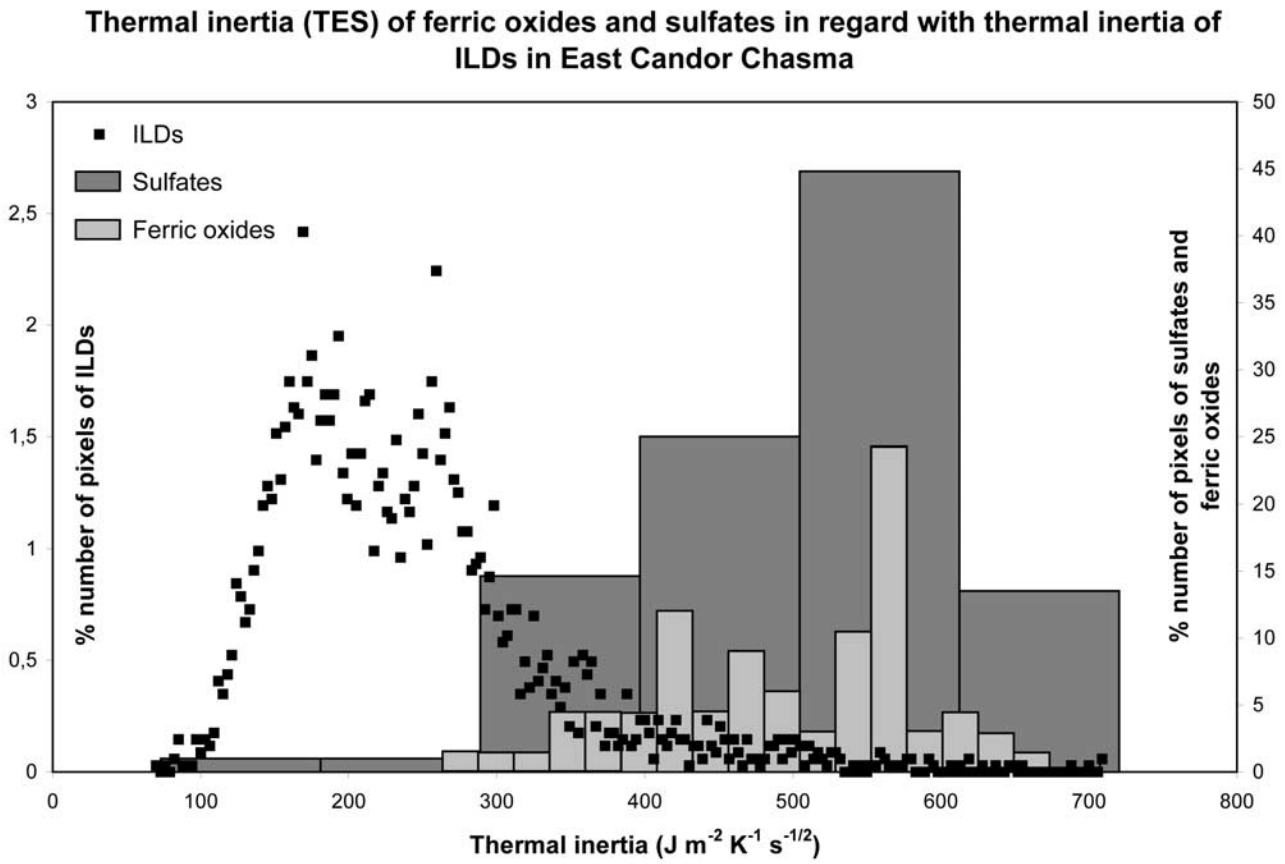

Figure 7. Statistical distribution of thermal inertia of ILDs, ferric oxides and sulfates in East Candor Chasma, computed from the TES thermal inertia map of *Putzig et al.* [2005] (Figure 6c). Thermal inertia values for areas where we have identified spectral signatures of sulfates and ferric oxides (robust detections only) are represented by dark and light grey boxes, respectively. Thermal inertia values for ILDs, as recognized visually by their morphology and structure on visible and IR images, are represented by black squares. Sulfate and ferric oxide distributions are displayed with larger class intervals than ILDs because they are detected on fewer pixels. ILDs are characterized by a large range of thermal inertia values (70–711 SI, with a mean of 240 SI, and most pixels between 130 and 300 SI). Thermal inertia values range from 127 to 667 SI (most pixels between 350 and 667 SI) for sulfate-rich sites and from 277 SI to 643 SI (485 SI on average) for ferric-oxide-rich sites. Thermal inertia of sulfate and ferric oxide-rich sites is usually higher than that of most ILDs. Where sulfates and ferric oxides are detected on ILDs, they correspond to ILDs with a high thermal inertia.

darker areas than the mottled materials to the SW and the ILDs to the North that indicates that site A has a lower temperature, hence has a lower thermal inertia. It is either less indurated or composed of finer grains, than the surrounding terrains. TES thermal inertia maps indicate an intermediate thermal inertia of 430 SI for site A (Figure 6c), which confirms that site A does not correspond to Martian dust which has a thermal inertia value smaller than ~200 SI. The dark dunes observed by MOC at site A (Figure 9c) suggest that the constituent material is sand.

[31] Site B (Figure 10) occupies an area of ~8.4 km by 3 km, at an elevation of −2600 m to −3600 m (Figure 10a). It is located on terrains of intermediate to low albedo (Figure 10b) corresponding to outcrops identified as ILDs, corroborating the interpretation made on the geological map by *Lucchitta* [1999] (Figure 10c). These ferric oxides-rich terrains have various brightness temperatures (Figure 10d). According to TES measurements, these terrains have gen-

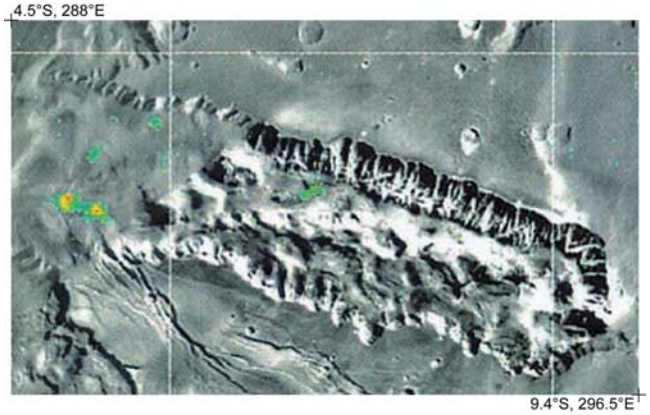

Figure 8. Distribution of gray crystalline hematite detected by TES in East Candor Chasma [*Christensen et al.*, 2001].

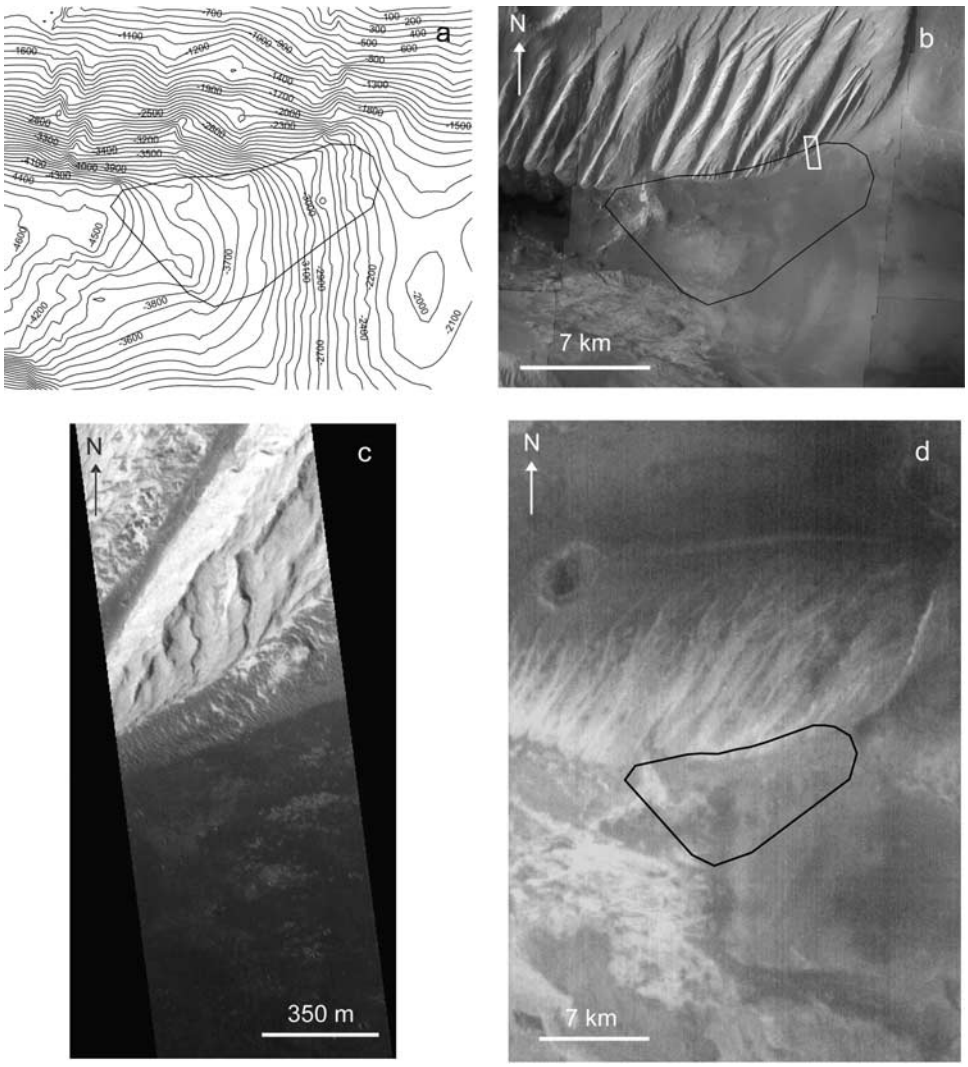

Figure 9. Detailed views of site A (288.8°E, 6.8°S) (location on Figure 5). (a) Elevation contours (interval 100 m) extracted from MOLA DEM. (b) Portion of THEMIS visible image (V09927002). (c) Part of MOC image M0900951. (d) Portion of THEMIS nighttime image I0747409. Site A contoured in black on Figures 9a, 9b and 9d. The white box in Figure 9b corresponds to the part of MOC image shown in Figure 9c.

erally an intermediate to low thermal inertia of 277 SI (Figure 6c).

[32] Site C (Figure 11) corresponds to a 700 m-high butte made of light-toned stratified layers (Figures 11a–11c) in which spectral signatures of sulfates have been observed (Figure 6a) [*Gendrin et al.*, 2005a, 2005b]. By comparison with the geological characteristics of ferric oxide-rich deposits at sites A and B, ferric oxides detected at site C may correspond to the dark material mantling the strata (black box on Figure 11c) and concentrated at its base (white box on Figure 11c), whereas sulfates may correspond to the stratified material. The dark material has accumulated in topographic lows and on benches; and in some cases it has been remobilized by the wind to form dunes (Figure 11c). The brightness temperature of this outcrop is significantly higher than that of the surrounding terrains (Figure 11d). TES thermal inertia maps indicate a high thermal inertia of 456 SI (Figure 6c), which is consistent with sandy material.

[33] Site D is located in the central part of East Candor Chasma (292.2°E, 6.7°S). It covers a ~50 km-long and 10 km-wide crescent-shaped area at the bottom of a large ILD escarpment (Figures 12a and 12b). This site is located in the lowest part of East Candor Chasma (−3500 m to −5300 m, Figure 12a). Ferric oxides are located on terrains of various (generally low) albedo (Figures 12b and 12c), and with various brightness temperatures (Figure 12d). Thermal inertia values for this site are commonly high (500 SI on average, Figure 6c).

[34] MOC images show that, at site D, a dark material forming both small dunes and larger smooth surfaces overlies a semicircular feature composed of light-toned stratified materials (Figures 12 and 13a–13c).

[35] This semicircular feature has a radius of 10 km and is composed of two morphologically distinct concentric parts. The southern (inner) part is convex-upward, with a mean surface slope of 10°, while the northern (outer) part has an average slope of 4°. Both parts display concentric terraces

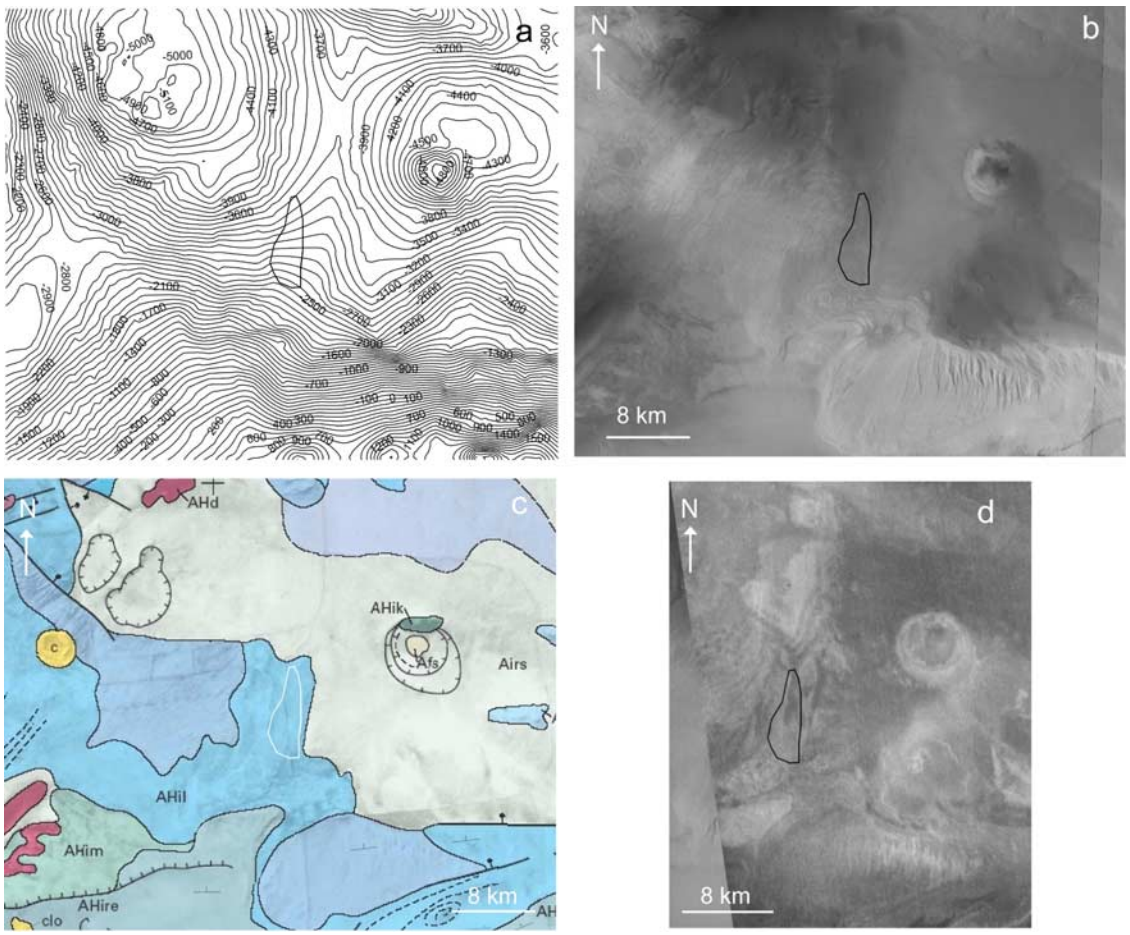

Figure 10. Detailed views of site B (289.0°E, 6.2°S) (location on Figure 5). (a) Elevation contours (interval 100 m) extracted from MOLA DEM. (b) Portion of HRSC image (orbit 0334). (c) Part of the geologic map of Ophir and Central Candor chasmata (MTM-05072) from *Lucchitta* [1999]. Map units: *Afs:* Chasma floor material, smooth material; *AHd:* Chasma floor material, dark material; *Airs:* Younger interior deposits, rolling and smooth material; *AHim:* Older interior deposits, mottled material; *AHire:* Older interior deposits, resistant material; *AHil:* Older interior deposits layered material; *C:* Crater material; *clo:* Outer ejecta lobe on some impact craters. (d) Portion of THEMIS nighttime image I07836016 overlying the HRSC image of (b). Site B contoured in black on Figures 10a, 10b, and 10d and in white on Figure 10c.

that are faintly visible in the topography. These surface slope values derived from MOLA DEM does not necessarily correspond to the dip angle of the beds.

[36] Fan-shaped deposits displaying concentric terraces have been observed elsewhere on Mars [*Ori et al.*, 2000; *Cabrol and Grin*, 2001; *Malin and Edgett*, 2003; *Irwin et al.*, 2005; *Di Achille et al.*, 2006; *Weitz et al.*, 2006], and have been interpreted as mass wasting deposits, alluvial fans or deltas, or the results of aeolian differential erosion. *Ori et al.* [2000] favored a delta origin, proposing that the terraces observed in the Memnonia region (Figure 13d) were formed by the action of waves in a standing body of water. Another morphologically similar fan has been reported in Coprates Catena, SE Valles Marineris (Figure 13e) by *Weitz et al.* [2006], who suggested that the fan formed as a delta in a lake that partially filled Coprates Catena. They explain the formation of terraces by shoreline erosion or decreases in water level in an ice-covered lake that partially filled Coprates Catena in the Hesperian period.

[37] A similar mode of formation can be proposed for the fan-shaped feature observed in East Candor Chasma. However, the absence of a visible feeding valley upstream (Figures 13a–13c) requires the zone of sedimentary transit and its flanks to be buried below the ILDs. The fan would thus have been emplaced before the deposition of the ILDs; it would have been buried below the ILDs and exhumed later, after the overlying ILDs had been eroded. If so, the preservation of the fan morphology suggests that the material composing the fan is significantly more resistant to erosion than the ILDs. Deep erosional flutes sculpt most ILDs, which is not observed on other Valles Marineris rock units (wallrock, landslide material, and other units such as this fan-shaped feature). This observation supports the hypothesis that the ILDs are significantly weaker than the other observed units and might be consistent with the hypothesis of an exhumed fan. In conclusion, this semicircular feature can be either (1) an erosional relict of a stratified formation stratigraphically underlying the ILDs

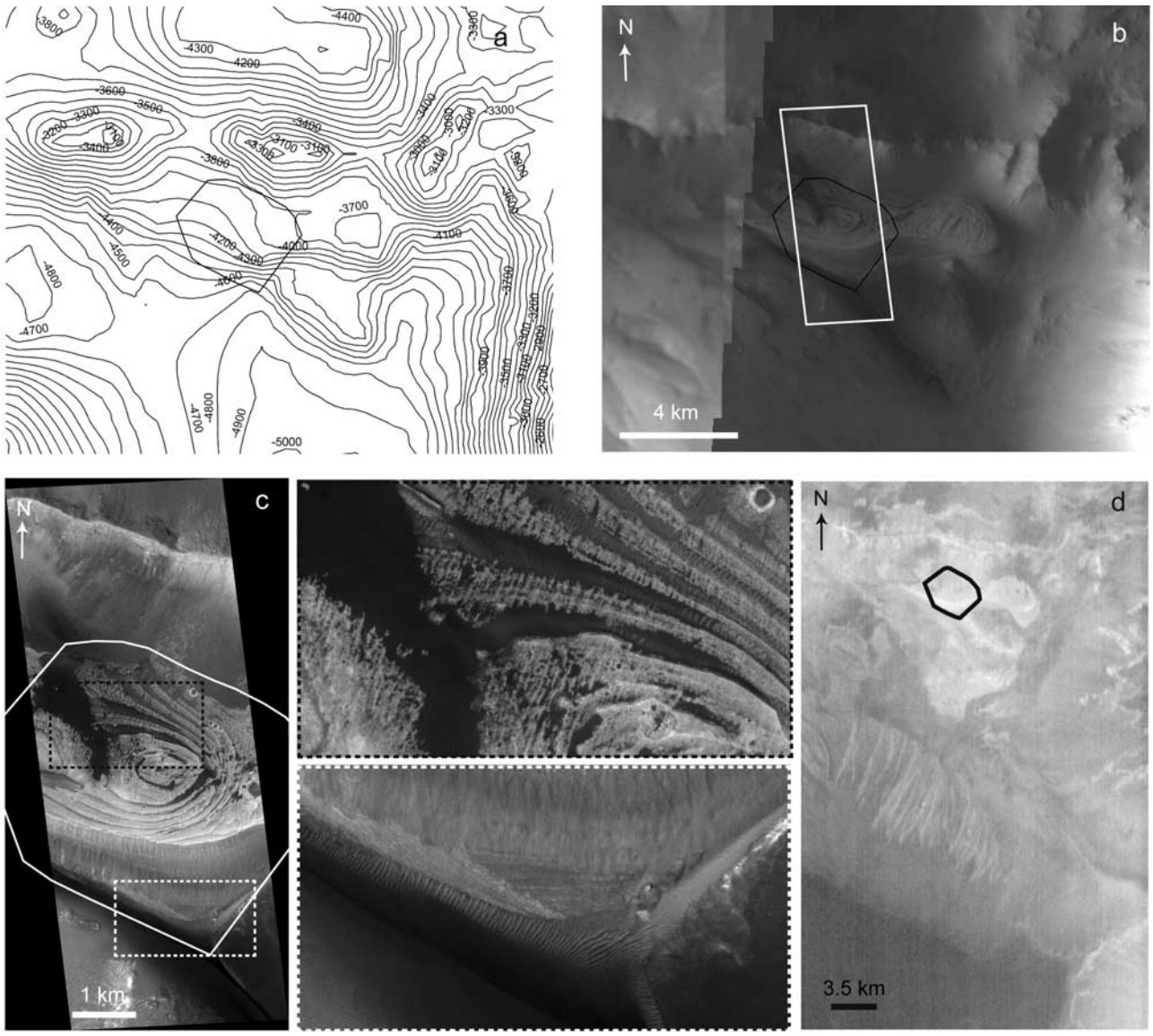

Figure 11. Detailed views of site C (290.7°E, 6.2°S) (location on Figure 5). (a) Elevation contours (interval 100 m) extracted from MOLA DEM. (b) Portion of THEMIS visible image (V06819001). The white box corresponds to the part of MOC image shown in Figure 11c. (c) Part of MOC image R0901074. (d) Portion of THEMIS nighttime image I0742413. Site C contoured in black on Figures 11a, 11b, and 11d and in white on Figure 11c.

(Figure 14b), (2) a sedimentary fan that has been buried by the ILDs and exhumed later (Figure 14c), or (3) an erosional relict of a former valley filling, stratigraphically overlying the ILDs (Figure 14d).

[38] Ferric oxide signatures are observed on the fan-shaped feature. Sulfates also have been detected here (Figure 6a) [*Gendrin et al.*, 2005a, 2005b]. As for sites A, B, and C, we suggest that sulfate signatures correspond to the light-toned stratified material, whereas ferric oxides signatures correspond to the overlying cover of dark sandy material. The occurrence of both ferric oxides and sulfates within the same sites (Figures 11 and 12) suggests a link in their formation process. A spatial correlation between ferric oxides and sulfates has been also observed in other regions of Valles Marineris, such as West Candor Chasma [*Mangold et al.*, 2005, 2008; *Murchie et al.*, 2007b, 2007c].

5. Origin of Ferric Oxides in East Candor Chasma

5.1. Results Synthesis

[39] Our analysis shows that ferric oxides are concentrated in scattered formations in East Candor Chasma and that they correspond to dark superficial material usually in the form of dunes or sand sheets. The surface of these formations lacks strong pyroxene signatures (Figure 6b), which suggests that they do not correspond to the high calcium pyroxene-rich dunes that are commonly found on Mars. Surfaces with ferric oxides have a mean thermal

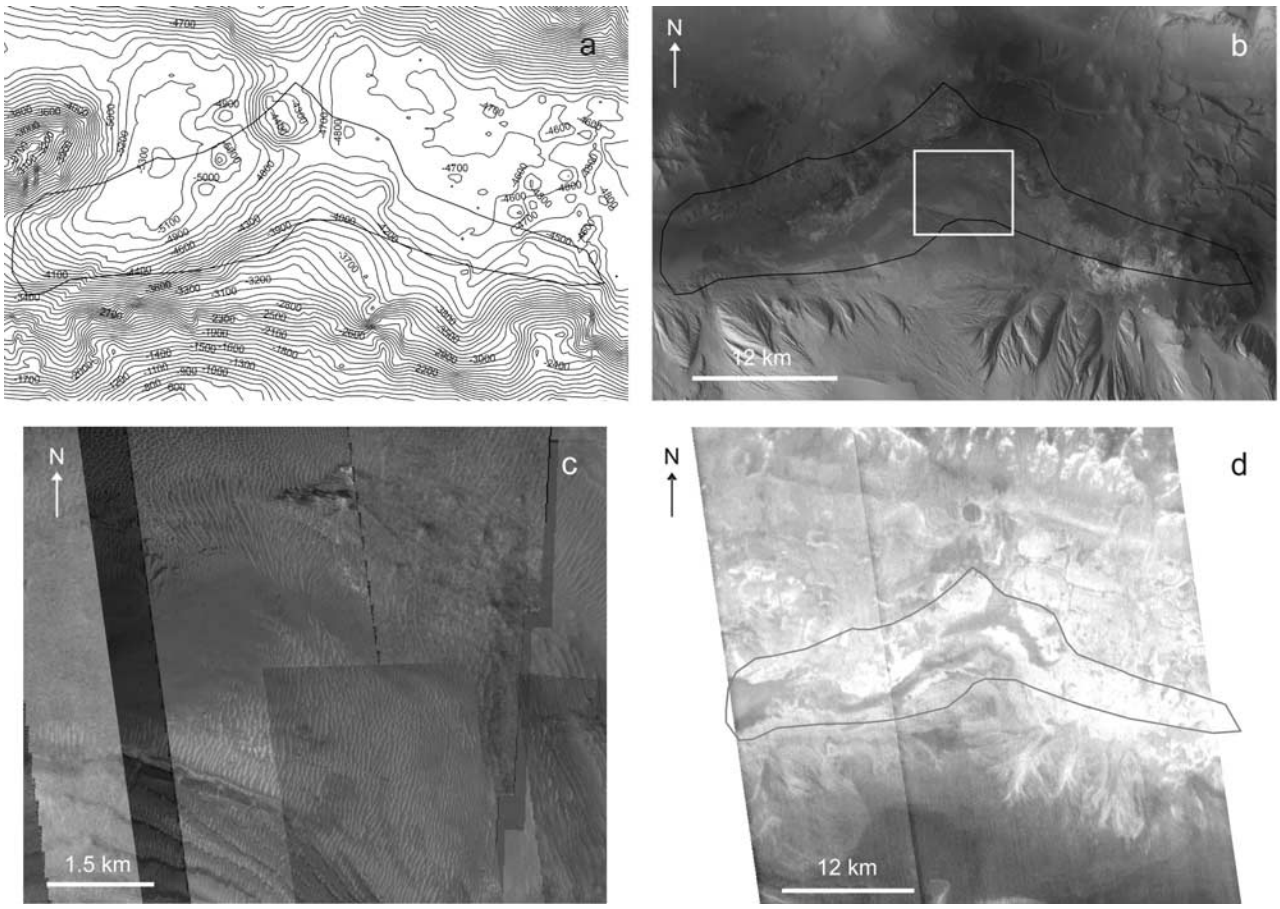

Figure 12. Detailed views of site D (292.2°E, 6.7°S) (location on Figure 5). (a) Elevation contours (interval 100 m) extracted from MOLA DEM. (b) Mosaic of HRSC images (orbits 2017 and 2028). (c) Mosaic of MOC images. (d) Mosaic of THEMIS nighttime images (I0665001, I07012013). Site D contoured in black on Figures 12a, 12b, and 12d. The white box in Figure 12b corresponds to the MOC mosaic shown in Figure 12c.

inertia value of 485 SI, which is consistent with surfaces partly composed of sandy material. These ferric oxide-rich sands are located in topographic lows between −5300 m for site D and −2050 m for site A. They form either sand accumulations at the foot of, or upon ILD escarpments, or a loose veneer on the ILDs.

5.2. Formation of Ferric Oxide Accumulations

[40] The ferric oxide-rich sands may be windblown material that was imported from other places of Valles Marineris or from elsewhere on Mars. Alternatively, they may have formed in situ without any significant transport. Their systematic association with ILDs suggests that they are genetically linked to the ILDs.

[41] On Mars, ferric oxides can form by aqueous alteration of mafic or ultramafic rocks [*King and McSween*, 2005] by hydrothermal fluids [*Newsom*, 1980], by low temperature solutions [e.g., *Bishop and Murad*, 1996; *McSween and Harvey*, 1998] or by magmatic acid fog (sulphuric-acid vapor) [i.e., *Morris et al.*, 1996; *Tosca et al.*, 2004]. For the first two leaching models, at a range of temperatures, volumes, and pH, the solutions become enriched in Mg, Na, Ca, SO_4, and Cl [*King et al.*, 2004]. The acid fog consists of a magmatic vapor composed of HCl and SO_2 whose interactions with H_2O at low temperature produce acid (pH < 4) solutions enriched in Mg, Fe, (Ca), SO_4, and Cl [*Hurowitz et al.*, 2006; *Tosca et al.*, 2005], from which ferric oxides can precipitate.

[42] At Meridiani Planum, the Opportunity rover has discovered dark spherules enriched in ferric oxides (gray hematite) embedded in and falling from light-toned sedimentary deposits enriched in Mg- and Fe-sulfates (jarosite) [*Klingelhöfer et al.*, 2004; *Bell et al.*, 2004; *Squyres and Knoll*, 2005; *Calvin et al.*, 2004; *Farrand et al.*, 2007]. Hematite is not only present in the concretions, but there is disseminated hematite in the sulfate-rich outcrop materials [*Morris et al.*, 2006]. *Squyres and Knoll* [2005] and *McLennan et al.* [2005] have suggested that the ferric oxides may have formed in these sulfate-rich rocks: they would have resulted from the dissolution of a Fe-rich sulfate (jarosite or polyhydrated sulfate) in the presence of groundwater table under changing chemical conditions [*Bigham and Nordstrom*, 2000; *Golden et al.*, 2005; *Tosca et al.*, 2005; *Clark et al.*, 2005; *McLennan et al.*, 2005].

[43] Noting that sulfates (monohydrated and polyhydrated sulfates) have been identified in the vicinity of ferric

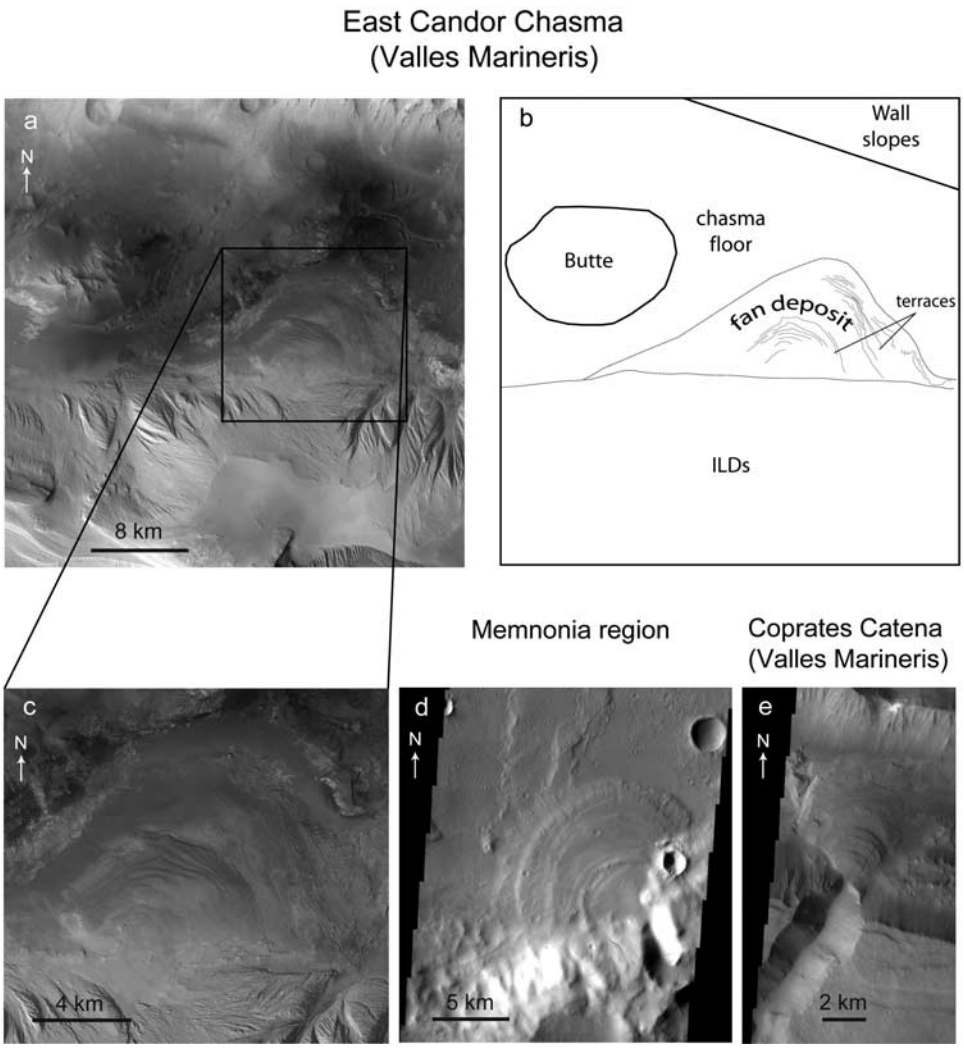

Figure 13. Fan-shaped deposits on Mars. (a) East Candor Chasma (this study): HRSC image (orbit 2028) (12.5 m/pixel). (b) Interpretation of Figure 13a. (c) Detail of Figure 13a. (d) Crater in Memnonia region: 8.6°S, 200.73°E (THEMIS visible image V10579001, 18 m/pixel). (e) Coprates Catena: 8.6°S, 200.73°E (THEMIS visible image, 18 m/pixel).

oxide deposits in Meridiani Planum as well as in East Candor Chasma, the diagenetic histories may be similar for both localities. However, no jarosite (Fe-sulfate) has been detected in East Candor Chasma or in any part of Valles Marineris so far. Unlike incomplete water-mediated diagenesis of jarosite in the Burns Cliff formation of Meridiani Planum [*Squyres and Knoll*, 2005], the diagenetic process in Valles Marineris may have endured long enough to dissolve all the jarosite, explaining why it is not spectrally visible at the surface. Also if the groundwater dissolved all the jarosite, it is difficult to explain why the other sulfates, such as Mg-sulfates would have been preserved. Alternatively, dust cover or insufficient spatial sampling with OMEGA may explain the lack of jarosite spectral signature, as discussed previously (section 4.2.1).

[44] We propose the following scenario for the accumulation of ferric oxides in the vicinity of sulfate-bearing ILDs in East Candor Chasma (Figure 14). First, the ILDs were deposited within the canyon. These layered deposits may be evaporites resulting from the precipitation of sulfates in bodies of water enriched in Mg, Ca, Fe, and SO_4 [e.g., *Squyres and Knoll*, 2005]. Alternatively, ILDs may be composed primarily of sedimentary or pyroclastic material, in which percolation of groundwater would have resulted in secondary precipitation of sulfates [e.g., *Gendrin et al.*, 2005a, 2005b]. We suggest that ferric oxides also precipitated in the ILDs. The iron required to form the ferric oxides would have been supplied by waters that were previously enriched in iron by dissolution of Fe-rich silicates or sulfates contained in the ILDs or in any other surrounding geological formation. Finally, the ferric oxide particles would have been separated from their matrix by aeolian and gravity-driven erosion of the ILDs, and would have accumulated in colluvial deposits at the foot of, or upon the erosional escarpments, and in loose residual veneers on the remaining ILDs. We observe red hematite in Candor Chasma, whereas gray hematite has been observed at the Opportunity landing site. Red hematite can be produced by crushing or abrading gray hematite [*Farrand et al.*, 2007]. Thus the red hematite observed in Candor Chasma may

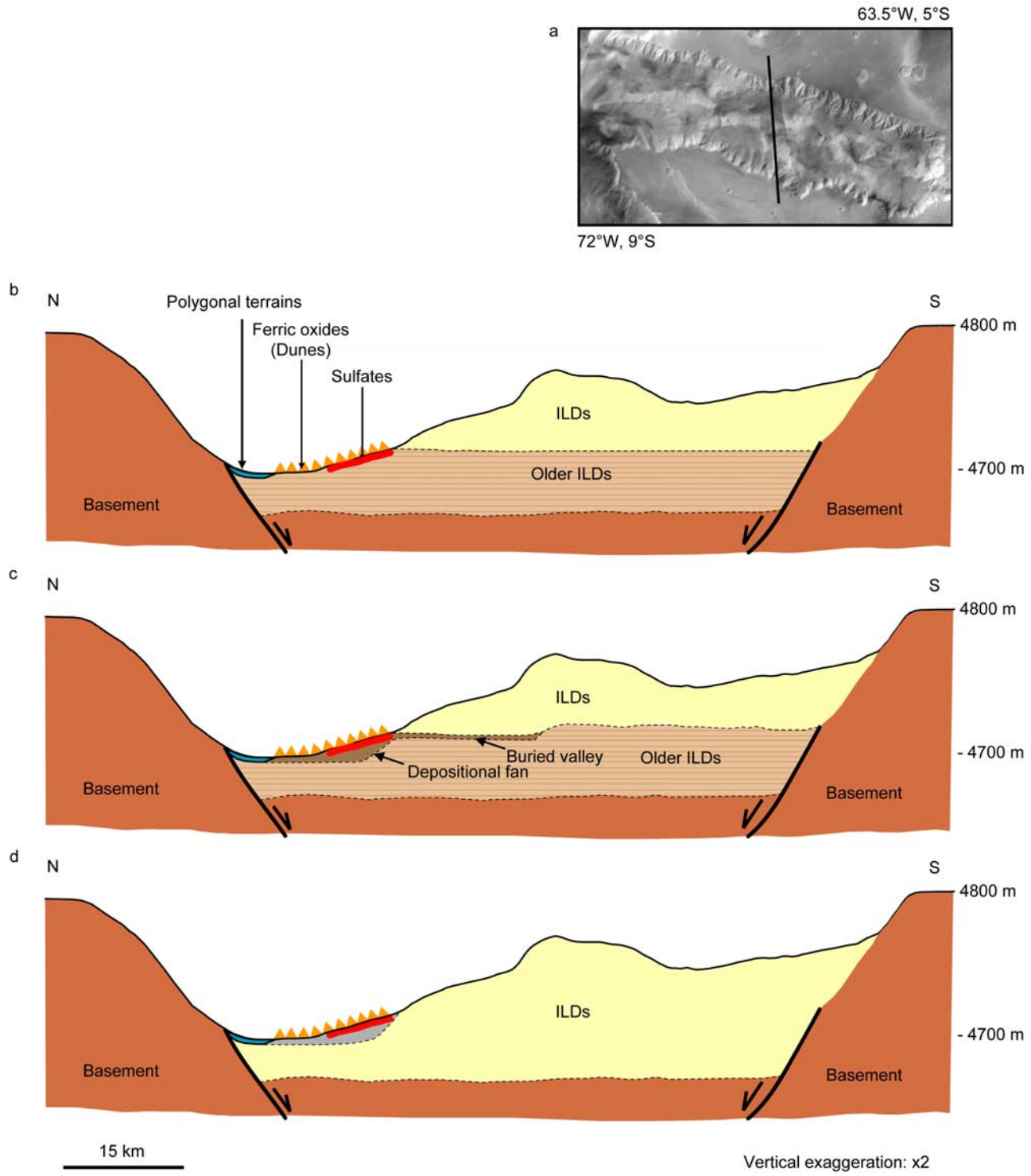

Figure 14. Three possible interpretations of a section across East Candor Chasma (topographic profile drawn from MOLA grid at 128 pixels per degree). (a) Location of cross-section on MOC mosaic (64 pixels/degree). The section crosses the semicircular feature of site D (Figure 13). (b) The semicircular feature is an erosional relict of a stratified formation underlying the ILDs. (c) It is a depositional fan that has been buried below the ILDs and exhumed later. (d) It is an erosional relict of a former valley infill, stratigraphically overlying the ILDs.

have been produced by natural abrasion, through aeolian activity or mass wasting, of gray hematite initially contained in the ILDs.

6. Conclusions

[45] We performed the analysis of OMEGA data using three different methods in order to detect and map ferric oxides in East Candor Chasma. Analysis of HRSC, THEMIS, MOC, HiRISE, TES and MOLA data for each site displaying a ferric signature has revealed the geological context of the ferric oxide deposits. They correspond to dunes or thin veneers of sand with generally high thermal inertia values (485 SI on average) and low albedo. They are systematically located in the vicinity of bright Interior Layered Deposits (ILDs). Some of the ferric oxide patches are located close to ILDs where monohydrated sulfates (such as the Mg-rich kieserite) and/or polyhydrated sulfates (Fe- and/or Mg-rich sulfates) have been detected. We propose a scenario for the accumulation of ferric oxides in East Candor Chasma, implying processes similar to those proposed for the Meridiani Planum Opportunity site [e.g., *Squyres and Knoll*, 2005; *McLennan et al.*, 2005]. Ferric oxides would have precipitated within the ILDs, from a solution previously enriched in Fe by leaching of iron-bearing silicates or sulfates. Then, the ferric oxide particles would have been separated from their matrix by aeolian and gravity-driven erosion of the ILDs, and would have accumulated in colluvial deposits at the foot of, or upon the erosional escarpments, and in loose residual veneers on the remaining ILDs. Some of the ferric oxide particles have been remobilized by winds to form dunes and have accumulated in topographic lows around the ILDs.

[46] **Acknowledgments.** We thank Ralph Milliken and William Farrand for their detailed and thoughtful reviews.

References

Bell, J. F., III, et al. (2004), Pancam multispectral imaging results from the Opportunity Rover at Meridiani Planum, *Science*, *306*, 1703–1709.

Bibring, J.-P., et al. (2004), OMEGA: Observatoire pour la Minéralogie, l'Eau, les Glaces et l'Activité, in *Mars Express: The Scientific Payload*, edited by A. Wison, *Eur. Space Agency Spec. Publ.*, *1240*, 37–39.

Bibring, J.-P., et al. (2005), Mars surface diversity as revealed by the OMEGA/Mars Express observations, *Science*, *307*, 1576–1581.

Bibring, J.-P., et al. (2006), Global mineralogical and aqueous Mars history derived from OMEGA/Mars Express data, *Science*, *312*, 400–404.

Bibring, J.-P. et al. (2007), Coupled ferric oxides and sulfates on the Martian surface, *Science*, *317*, 1206–1210.

Bigham, J. M., and D. K. Nordstrom (2000), Iron and aluminum hydroxysulfates from acid sulfate waters, in *Sulfate Minerals: Crystallography, Geochemistry and Environmental Significance*, edited by C. N. Alpers, J. L. Jambor, and D. K. Nordstrom, pp. 351–403, Mineral. Soc. of Am. / *Geochem. Soc.*, Washington, D. C.

Bishop, J. L., and E. Murad (1996), Schwertmannite on Mars? Spectroscopic analyses of schwertmannite, its relationship to other ferric minerals, and its possible presence in the surface material on Mars, in *Mineral Spectroscopy: A Tribute to Roger G. Burns*, edited by M. D. Dyar, C. A. McCammon, and M. W. Schaefer, *Spec. Publ. Geochem. Soc.*, *5*, 337–358.

Boardman, J. W. (1989), Inversion of imaging spectrometry data using singular value decomposition, in *Proceedings, IGARSS'89*, *12th Canadian Symposium on Remote Sensing*, vol. 4, pp. 2069–2072, Vancouver, B. C.

Boardman, J. W. (1992), Sedimentary facies analysis using imaging spectrometry: A geophysical inverse problem, Ph.D. thesis, Univ. of Colorado, Boulder, Colo., p. 212.

Boardman, J. W., F. A. Kruse, and R. O. Green (1995), Mapping target signatures via partial unmixing of AVIRIS data, in *Summaries of the Fifth JPL Airborne Earth Science Workshop*, vol. 1, pp. 23–26, *JPL Publ. 95-1*, Washington, D. C.

Cabrol, N. A., and E. A. Grin (2001), The evolution of lacustrine environments on Mars: Is Mars only hydrologically dormant?, *Icarus*, *149*, 291–328.

Calvin, W., et al. (2004), "Blueberries": A summary of the hematite concretions found at the Opportunity landing site, *Sec. Conf. Early Mars*, 8074.

Chapman, M. G., and K. L. Tanaka (2001), Interior trough deposits on Mars: Subice volcanoes?, *J. Geophys. Res.*, *106*(E5), 10,087–10,100.

Christensen, P. R., D. L. Anderson, S. C. Chase, R. N. Clark, H. H. Kieffer, M. C. Malin, J. C. Pearl, J. Carpenter, N. Bandiera, and F. G. Brown (1992), Thermal emission spectrometer experiment – Mars Observer mission, *J. Geophys. Res.*, *97*(E5), 7719–7734.

Christensen, P. R., R. V. Morris, M. D. Lane, J. L. Bandfield, and M. C. Malin (2001), Global mapping of Martian hematite mineral deposits: Remnants of water-driven processes on early Mars, *J. Geophys. Res.*, *106*(E10), 23,873–23,886.

Christensen, P. R., et al. (2004), The Thermal Emission Imaging System (THEMIS) for the Mars 2001 Odyssey mission, *Space Sci. Rev.*, *110*(1), 85–130, doi:10.1023/B.SPAC.0000021008.16305.94.

Clark, R. N., G. A. Swayze, A. Gallagher, T. V. V. King, and W. M. Calvin (1993), *The U. S Geological Survey, Digital Spectral Library, Version 1: 0.2 to 3.0 μm*, *USGS Open File Rep. 93–592*, 1326 pp., *U.S. Geol. Surv.*, Washington, D.C.

Clark, R. N., and G. A. Swayze (1995), Automated spectral analysis: Mapping minerals, amorphous materials, environmental materials, vegetation, water, ice and snow, and other materials: The USGS Tricorder Algorithm, *Lunar Planet. Sci.*, *XXVI*, 255–256.

Clark, B. C., et al. (2005), Chemistry and mineralogy of outcrops at Meridiani Planum, *Earth Planet. Sci. Lett.*, *240*, 73–94.

Clark, R. N., G. A. Swayze, R. Wise, K. E. Livo, T. M. Hoefen, R. F. Kokaly, and S. J. Sutley (2003), A digital spectral library for planetary and terrestrial spectroscopy analysis, in *American Astronomical Society, 35th DPS Meeting, #19.03; Bulletin of the American Astronomical Society*, vol. 35, p. 948.

Combe, J.-Ph. (2005), Études des surfaces planétaires par télédétection visible-infrarouge hyperspectrale, Ph.D. thesis, 300 pp., Université des Nantes, France.

Combe, J.-Ph., S. Le Mouélic, C. Sotin, A. Gendrin, L. Le Deit, J. F. Mustard, J.-P. Bibring, B. Gondet, Y. Langevin, and The Omega Science Team (2006), Analysis of OMEGA/Mars Express hyperspectral data using a linear unmixing model: Method and preliminary results, *Lunar Planet. Sci.*, *XXXVII*, Abstract 2010.

Combe, J.-P., et al. (2008), Analysis of OMEGA/Mars express data hyperspectral data using a multiple-endmember linear spectral unmixing model (MELSUM): Methodology and first results, *Planet. Space Sci.*, *56*(7), 951–975, doi:10.1016/j.pss.200712.007.

Crowley, J. K. (1991), Visible and near-infrared (0.4–2.5 m) reflectance spectra of playa evaporite minerals, *J. Geophys. Res.*, *96*(B10), 16,231–16,240.

Di Achille, G., G. G. Ori, D. Reiss, E. Hauber, K. Gwinner, G. Michael, and G. Neukum (2006), A steep fan at Coprates Catena, Valles Marineris, Mars, as seen by HRSC data, *Geophys. Res. Lett.*, *33*, L07204, doi:10.1029/2005GL025435.

Irwin, R. P., A. D. Howard, R. A. Craddock, and J. M. Moore (2005), An intense terminal epoch of widespread fluvial activity on early Mars: 2. Increased runoff and paleolake development, *J. Geophys. Res.*, *110*, E12S15, doi:10.1029/2005JE002460.

Farrand, W. H., et al. (2007), Visible and near-infrared multispectral analysis of rocks at Meridiani Planum, Mars, by the Mars Exploration rover Opportunity, *J. Geophys. Res.*, *112*, E06S02, doi:10.1029/2006JE002773.

Gendrin, A., et al. (2005a), Identification of predominant ferric signatures in association to the Martian sulfate deposits, *Lunar Planet. Science*, *XXXVI*, Abstract 1378.

Gendrin, A., et al. (2005b), Sulfates in Martian layered terrains: The OMEGA/Mars Express view, *Science*, *307*, 1587–1591.

Golden, D. C., D. W. Ming, R. V. Morris, and S. A. Mertzman (2005), Laboratory-simulated acid-sulfate weathering of basaltic materials: Implications for formation of sulfates at Meridiani Planum and Gusev Crater, Mars, *J. Geophys. Res.*, *110*, E12S07, doi:10.1029/2005JE002451.

Hurowitz, J. A., S. M. McLennan, N. J. Tosca, R. Arvidson, J. R. Michalski, D. W. Ming, C. Schröder, and S. W. Squyres (2006), In situ and experimental evidence for acidic weathering of rocks and soils on Mars, *J. Geophys. Res.*, *111*(E2), E02S19, doi:10.1029/2005JE002515.

Kieffer, H. H., S. C. Chase Jr., E. Miner, G. Münch, and G. Neugebauer (1973), Preliminary report on infrared radiometric measurements from the Mariner 9 spacecraft, *J. Geophys. Res.*, *78*(20), 4291–4312.

King, P. L., D. T. Lescinsky, and H. W. Nesbitt (2004), The composition and evolution of primordial solutions on Mars, with application to other planetary bodies, *Geochim. Cosmochim. Acta*, *68*, 4993–5008.

King, P. L., and H. Y. McSween (2005), Effects of H2O, pH, and oxidation state on the stability of Fe minerals on Mars, *J. Geophys. Res.*, *110*(E12), E12S10, doi:10.1029/2005JE002482.

Klingelhöfer, G., et al. (2004), Jarosite and Hematite at Meridiani Planum from opportunity's Mossbauer spectrometer, *Science*, *306*(5702), 1740–1745, doi:10.1126/science.1104653.

Knudson, A. T., R. E. Arvidson, P. R. Christensen, S. L. Murchie, J. F. Mustard, L. H. Roach, C. M. Weitz, S. M. Wiseman, and the CRISM Science Team (2007), Aqueous geology in Valles Marineris: New insights in the relationship of hematite and sulfates from CRISM and HiRISE, in *Seventh International Martian Conference on Mars*, vol. 1353, Abstract 3370.

Komatsu, G., G. G. Ori, P. Ciarcelluti, and Y. D. Litasov (2004), Interior layered deposits of Valles Marineris, Mars: Analogous subice volcanism related to Baikal Rifting, Southern Siberia, *Planet. Space. Sci.*, *52*, 167–187.

Kruse, F. A., A. B. Lefkoff, J. B. Boardman, K. B. Heidebrecht, A. T. Shapiro, P. J. Barloon, and A. F. H. Goetz (1993), The spectral image processing system (SIPS) - Interactive visualization and analysis of imaging spectrometer data: Remote sensing of environment, *Special issue on AVIRIS*, *44*, 145–163.

Langevin, Y., F. Poulet, J.-P. Bibring, and B. Gondet (2005), Sulfates in the north polar region of Mars detected by OMEGA/Mars Express, *Science*, *307*, 1584–1586.

Lucchitta, B. K. (1990), Young volcanic deposits in the Valles Marineris Mars?, *Icarus*, *86*(2), 476–509, doi:10.1016/0019-1035(90)90230-7.

Lucchitta, B. K., A. S. McEwen, G. D. Clow, P. E. Geissler, R. B. Singer, R. A. Schultz, and S. W. Squyres (1992), The canyon system on Mars, in *Mars*, *Univ. of Arizona*, Tucson, 453–492.

Lucchitta, B. K. (1999), Geologic map of Ophir and Central Candor Chasmata (MTM-05072), USGS Map I-2568.

Malin, M. C., G. E. Danielson, A. P. Ingersoll, H. J. Veverka, M. A. Ravine, and T. A. Soulanille (1992), Mars Observer camera, *J. Geophys. Res.*, *97*(E5), 7699–7718.

Malin, M. C., and K. S. Edgett (2003), Evidence for persistent flow and aqueous sedimentation on early Mars, *Science*, *302*, 1931–1934.

Mangold, N., A. Gendrin, C. Quantin, B. Gondet, Y. Langevin, and J.-P. Bibring (2005), Analysis of Candor Chasma interior layered deposits from OMEGA/MEx spectra, *Lunar Planet. Sci.*, *XXXVI*, Abstract 1330.

Mangold, N., A. Gendrin, B. Gondet, S. Le Mouélic, C. Quantin, V. Ansan, J.-P. Bibring, Y. Langevin, P. Masson, and G. Neukum (2008), Spectral and geological study of the sulfate-rich region of West Candor Chasma, Mars, *Icarus*, *194*(2), 519–543, doi:10.1016/j.icarus.2007.10.021.

McCauley, J. F., M. H. Carr, J. A. Cutts, W. K. Hartmann, H. Masursky, D. J. Milton, R. P. Sharp, and D. E. Wilhelms (1972), Preliminary mariner 9 report on the geology of Mars, *Icarus*, *17*, 289–327.

McLennan, S. M., et al. (2005), Provenance and diagenesis of the evaporite-bearing Burns formation, Meridiani Planum Mars, *Earth Planet. Sci. Lett.*, *240*, 95–121.

McSween, H. Y., Jr., and R. P. Harvey (1998), An evaporation model for formation of carbonates in the ALH84001 Martian meteorite, *Int. Geol. Rev.*, *40*, 774–783.

Mellon, M. T., B. M. Jakosky, H. H. Kieffer, and P. R. Christensen (2000), High resolution thermal inertia mapping from the Mars Global Surveyor thermal emission spectrometer, *Icarus*, *148*, 437–455.

Morris, R. V., D. W. Ming, D. C. Golden, and J. F. Bell (1996), An occurrence of jarositic tephra on Mauna Kea, Hawaii: Implications for the ferric mineralogy of the Martian surface, in *Mineral Spectroscopy: A Tribute to Roger G. Burns*, edited by M. D. Dyar, C. McCammon, and M. W. Schaefer, *Spec. Publ. Geochem. Soc.*, *5*, 327–336.

Morris, R. V., et al. (2006), Mössbauer mineralogy of rock, soil, and dust at Meridiani Planum, Mars: Opportunity's journey across sulfate-rich outcrop, basaltic sand and dust, and hematite lag deposits, *J. Geophys. Res.*, *111*, E12S15, doi:10.1029/2006JE002791.

Murchie, S., et al. (2003), CRISM: Compact reconnaissance imaging spectrometer for Mars on the Mars reconnaissance orbiter, in *Sixth International Conference on Mars*, Abstract 3062.

Murchie, S., et al. (2007a), Compact reconnaissance imaging spectrometer for Mars (CRISM) on Mars Reconnaissance Orbiter (MRO), *J. Geophys. Res.*, *112*(E5), E05S03, doi:10.1029/2006JE002682.

Murchie, S., et al. (2007b), First CRISM observations of layered material in Western Candor Chasma, *Lunar Planet. Sci.*, *XXXVIII*, Abstract 1476.

Murchie, S., L. Roach, R. Milliken, F. Seelos, S. Wiseman, D. Humm, J. Mustard, J.-P. Bibring, and the CRISM Science Team (2007c), Spectral mapping of interior layered deposits of Western Candor Chasma by CRISM, *Eos Trans. AGU*, Fall Meet., Abstract P21C-04.

Mustard, J. F., and J. M. Sunshine (1999), Spectral analysis for Earth science: Investigation using remote sensing data, in *Remote Sensing for the Earth Science: Manual of Remote Seinsing*, 3rd ed., vol. 3, edited by N. Andrew Rencz, John Wiley, Hoboken, N. J.

Mustard, J. F., S. Murchie, S. Erard, and J. Sunshine (1997), In situ compositions of Martian volcanics: Implications for the mantle, *J. Geophys. Res.*, *102*(E11), 25,605–25,615.

Mustard, J. F., F. Poulet, A. Gendrin, J.-P. Bibring, Y. Langevin, B. Gondet, N. Mangold, G. Bellucci, and F. Altieri (2005), Olivine and pyroxene diversity in the crust of Mars, *Science*, *307*, 1594–1597.

Nedell, S. S., and S. W. Squyres (1987), Formation of the layered deposits in the Valles Marineris, Mars, in *Lunar and Planetary Inst., MECA Symposium on Mars: Evolution of its Climate and Atmosphere*, pp. 88–90.

Neukum, G., and R. Jaumann (2004), HRSC: The high resolution stereo camera of Mars express, in *Mars Express: The Scientific Payload, ESA SP-1240*, pp. 17–35.

Newsom, H. E. (1980), Hydrothermal alteration of impact melt sheets with implications for Mars, *Icarus*, *44*, 207–216.

Ori, G. G., L. Marinangeli, and A. Baliva (2000), Terraces and Gilbert-type deltas in crater lakes in Ismenius Lacus and Memnonia (Mars), *J. Geophys. Res.*, *105*(E7), 17,629–17,641.

Peulvast, J.-P., D. Mège, J. Chiciak, F. Costard, and P. L. Masson (2001), Morphology, evolution and tectonics of Valles Marineris wallslopes (Mars), *Geomorphology*, *37*, 329–352.

Putzig, N. E., M. T. Mellon, K. A. Kretke, and R. E. Arvidson (2005), Global thermal inertia and surface properties of Mars from the MGS mapping mission, *Icarus*, *173*, 325–341.

Quantin, C., P. Allemand, N. Mangold, and C. Delacourt (2004), Ages of Valles Marineris (Mars) landslides and implications for canyon history, *Icarus*, *172*, 555–572.

Ramsey, M. S., and P. R. Christensen (1998), Mineral abundance determination: Quantitative deconvolution of thermal emission spectra, *J. Geophys. Res.*, *103*(B1), 577–596.

Sabol, D. E., Jr., J. B. Admas, and M. O. Smith (1992), Quantitative subpixel spectral detection of targets in multispectral images, *J. Geophys. Res.*, *97*(E2), 2659–2672.

Seidelmann, P. K., et al. (2002), Report of the IAU/IAG working group on cartographic coordinates and rotational elements of the planets and satellites: 2000, *Celestial Mech. Dyn. Astron.*, *82*, 83–110.

Smith, D. E., et al. (2001), Mars Orbiter Laser Altimeter (MOLA): Experiment summary after the first year of global mapping of Mars, *J. Geophys. Res.*, *106*, 23,689–23,722.

Squyres, S. W., and A. H. Knoll (2005), Sedimentary rocks at Meridiani Planum: Origin, diagenesis, and implications for life on Mars, *Earth Planet. Sci. Lett.*, *240*(1), 1–10.

Sunshine, J., et al. (1990), Deconvolution of mineral absorption bands: An improved approach, *J. Geophys. Res.*, *95*(B5), 6955–6966.

Tosca, N. J., S. M. McLennan, D. H. Lindsley, and M. A. A. Schoonen (2004), Acid-sulfate weathering of synthetic Martian basalt: The acid fog model revisited, *J. Geophys. Res.*, *109*, E05003, doi:10.1029/2003JE002218.

Tosca, N. J., S. M. McLennan, B. C. Clark, J. P. Grotzinger, J. A. Hurowitz, A. H. Knoll, C. Schröder, and S. W. Squyres (2005), Geochemical modeling of evaporation processes on Mars: Insight from the sedimentary record at Meridiani Planum, *Earth Planet. Sci. Lett.*, *240*, 122–148.

Weitz, C. M., R. P. Irwin III, F. C. Chuang, M. C. Bourke, and D. A. Crown (2006), Formation of a terraced fan deposit in Coprates Catena Mars, *Icarus*, *184*, 436–451.

J.-P. Bibring and A. Gendrin, Institut d'Astrophysique Spatiale, CNRS, Université Paris 11, Bâtiment 121, 91405 Orsay Campus, France.

O. Bourgeois, L. Le Deit, S. Le Mouélic, N. Mangold, D. Mège, and C. Sotin, Laboratoire de Planétologie et Géodynamique de Nantes, UMR 6112, CNRS, Université de Nantes, Faculté des Sciences et Techniques, 2 chemin de la Houssinière BP 92208, 44322 Nantes Cedex 3, France. (laetitia.ledeit@univ-nantes.fr)

J. P. Combe, Space Science Institute, Bear Fight Center, 22 Fiddler's Road, P. O. Box 667, Winthrop, WA 98862, USA.

E. Hauber, Institute of Planetary Research, German Aerospace Center (DLR), Rutherfordstr. 2, Berlin, 12489, Germany.